Medical Image Segmentation with Shape Priors

DISSERTATION
zur Erlangung des Doktorgrades der Technischen Fakultät der
Albert-Ludwigs-Universität Freiburg im Breisgau

vorgelegt von
Esmeralda Ruiz Pujadas
aus Barcelona

2013

Dekan

Prof. Dr. Manoli

Gutachter

Prof. Dr. Thomas Brox

Prof. Dr. Jürgen Hennig

Beisitz

Prof. Dr. Reindl

Vorsitz

Prof. Dr. H. Burkhardt

Tag der Prüfung

16.01.2014

Autor

Esmeralda Ruiz Pujadas

Medical Physics
Department of Radiology
University Hospital Freiburg

Medical Image Segmentation with Shape Priors

by

Esmeralda Ruiz Pujadas

Submitted to the Faculty of Engineering; Department of Computer Science
in 2013, in partial fulfillment of the
requirements for the degree of
PhD in Engineering

Abstract

In dieser Arbeit wurden zwei neue Methoden zur Segmentierung von biomedizinschen Bildern implementiert. Hierbei wurde sich vorallem auf das Herz konzentriert, die Methoden können aber natürlich auch auf andere Daten angewandt werden. The erste Technik basiert auf 'Normalized Cuts' und präsentiert einen neuen Weg Vorwissen einzubringen. Das Vorwissen wird direkt in die Kostenfunktion integriert und bevorzugt Segmentierungen, die möglichst ähnlich zu einer groben Vorsegmentierung sind. Es können auf diese Art auch komplexere Formmodelle eingebracht werden. Getestet wurde diese Methode auf sowohl biomedizinischen Daten, als auch auf Fotographien natürlicher Szenen. Es konnte gezeigt werden, dass auch bei sehr ungenauem Vorwissen die Methode vielversprechende Ergebnisse erzielen kann. In einem zweiten Ansatz wurden sogennante 'Level Sets' durch nicht-Euklidsche Basis Funktionen erweitert. Das Vorwissen wurde mittels probabilistischer Karten repräsentiert. Die Experimente zeigen einige Vorteile dieser Methode, allerdings auch Probleme, die durch die Kombination beider Methoden entstehen können.

Acknowledgments

First and foremost, I would like to thank my parents Inés Pujadas and José Manuel Ruiz and grandparents María del Tremedal and Francisco for all the support throughout my PhD. Without their support and strength, I do not think I would have concluded it. I would also like to sincerely thank my supervisor Dr. Reisert as well as my supervisor Prof. Bai Li from my PhD stay, for their guidance and support throughout this study. I would also like to thank Prof. Brox for serving as a member on my thesis committee. His comments and suggestions were very beneficial in my completion of the manuscript. Moreover, I would like to acknowledge Prof. Hennig for all his help during my PhD. And last but not least, to all my friends who encouraged me to continue as well as my colleagues from work Dr. Ute Ludwig and David Pilutti who gave me a hand everytime I needed it.

Finally, I would like to mention that this work has been funded by the European Commission under the MIBISOC project in the Marie Curie Initial Training Network.

Contents

1 Introduction **15**

1.1 Thesis Outline 17

1.2 Description of Short-axis MR Images 17

1.3 Issues in Cardiac MR Image Segmentation 19

2 Review of Segmentation Methods **21**

2.1 Introduction 21

2.2 Model-free Segmentation 22

2.3 Snakes 23

2.4 Level Sets 28

2.5 Active Shape Models 32

2.6 Graph Cuts 35

2.7 Atlas-based Segmentation 38

2.8 Convex Optimization 39

2.9 Conclusion 44

3 Shape Model Techniques **47**

3.1 Shape and Landmarks 47

3.2 Procrustes for Shape Alignment 48

3.3 Modelling Shape Variations 50

3.4 Statistical Shape Models 55

3.5 Shape Model for Prior Computation 56

4 Normalized Cuts with Shape Priors **59**

4.1 Introduction 59

4.2 Theory 61

4.2.1 Introducing the Prior 62

4.2.2 Spectral Relaxation 64

4.3 Implementation 66

4.4 Experimental Evaluation 66

4.4.1 Segmentation of Biomedical Data 67

4.4.2 Segmentation of People 71

4.5 Conclusions 73

5 Non-Euclidean Basis-based Level Sets with Shape Prior **75**

5.1 Introduction 75

5.2 Radial Basis Functions 77

5.3 Level Set with Radial Basis Functions 79

5.4 Non-Euclidean Radial Basis 81

5.5 Fast Marching 83

5.6 Region and Shape Prior Definition 85

5.7 Validation 87

5.8 Conclusion 89

6 Conclusions **91**

Authors' contribution **93**

List of Figures

1-1 The heart wall is divided into three layers: epicardium, myocardium, and endocardium. 18

1-2 Three slices in short axis view were acquired: basal, mid-ventricular, and apical. (Author: Bernd Jung) 18

1-3 Cardiac MR image: the Region Of Interest (ROI) is obtained to get the segmentation of the myocardium (white) located between the epicardium and the endocardium. (Author: Bernd Jung) 19

1-4 Cardiac images corresponding to 12 short-axis slices from apex to base. (Author: Petitjean) 20

2-1 Segmentation of the left ventricle using snakes. The initial contour is plotted in grey and the final converged result is plotted in white. (Author: Chenyang Xu et al.) 23

2-2 Level set methodology and curve propagation. The left column shows the evolving level set function, while, on the right, the corresponding curve that is the zero level set values of the surface is illustrated. (Author: Nikos Paragios et al.) 29

2-3 Effect of varying the first shape parameter around the average shape. (Author: T. F. Cootes) 34

2-4 Example of graph-based image segmentation. 36

2-5 An example of the Ford-Fulkerson method. 37

2-6 Registration of a cardiac atlas in form of a labelled image to a MR image of the heart. (Author: M. Lorenzo-Valdes) 39

2-7 Approximation of a non-convex function in a convex one. (Author: Thomas Brox) 40

2-8 Process of convex optimization. u is the solution of the original problem and w the solution to the relaxed problem. The projected solution $\pi(w)$ to the original problem is not the global optimal solution of the original problem. (Author: Bastian Goldlucke) 41

2-9 (a) The two-label case: A binary function θ is used to partition the image domain Ω into two regions. (b) The three-label case: Two binary functions $\theta_1 \geq \theta_2$ are used to partition the image domain Ω into three regions. (Author: Cremers) 41

3-1 Procrustes example between two shapes showing intermediate results after translation, scaling and rotation. (Author: Alex Townsend) . . . 49

3-2 PCA example in 2D: The principal components of a data set are its major axes. (Author: Swan and Sandilands) 50

3-3 PCA procedure: Rotates data to its major axes preserving original distances between data points and removing correlations between variables. 54

3-4 Example of the proposed PCA which gives as a first component the average shape and the shape variation for the rest of components. . . 56

4-1 Example of using the principal components as a shape prior. 64

4-2 Segmentation of the left ventricle. (a) Original image. (b) Our method with its corresponding ncut-vector. (c) Partial grouping. (d) Intensity based-Bias Ncut. (e) Intervening contour based-Bias Ncut. 68

4-3 Segmentation of the heart. (a) Original image with single prior. (b) Our method and its normalized cut. (c) Partial grouping by Yu's method. (d) Intensity based-Bias Ncut. (e) Intervening contour based-Bias Ncut. 69

4-4 Segmentation of the myocardium with our method. (a) Original images. (b) Segmentation in white. 70

4-5 Segmentation of colour images using the poselet object detector output as a prior for the proposed approach (New) with its corresponding normalized cut (Ncut), (BNC_{ic}) Intervening contour based-Bias Ncut and (PG) Partial Grouping. 72

5-1 The effect of the non-Euclidean distance metric. (a) Original Image with a RBF center in the middle. (b) Spherical-shaped RBF with $\beta = 0$. (c) Increasing the non-Euclidean part of the metric from left to right with $\beta > 0$. 81

5-2 Comparison of Non-Euclidean RBFs versus Euclidean RBFs. (a) Original image. (b) Initial level set using Euclidean Distance. (c) Segmentation using Euclidean RBFs. (d) Initial level set using Non-Euclidean Distance. (e) Segmentation using Non-Euclidean RBFs. 82

5-3 Example of spatial shape prior. Given N training images an average image is computed as a spatial prior which is aligned to the target image and used as a probabilistic map for the level set segmentation. 87

5-4 Segmentation of the myocardium using our approach with two different patients: a) Original data sets. b) Segmentation in white. 88

5-5 Comparison of methods: Non-Euclidean Basis Functions, Euclidean RBFs and the ordinary Level Sets. 89

List of Tables

4.1 Average performance measures for the left ventricle, for the proposed approach (New), (PG) Partial Grouping, (BNC_i) Intensity based-Biased Ncut, (BNC_{ic}) Intervening contour based-Bias Ncut. 68

4.2 Average performance measures for cardiac sequences, for the proposed approach (New), (PG) Partial Grouping, (BNC_i) Intensity based-Biased Ncut, (BNC_{ic}) Intervening contour based-Bias Ncut. 69

4.3 Average performance measures for colour images, for the proposed approach (New), (PG) Partial Grouping, (BNC_i) Intensity based-Biased Ncut, (BNC_{ic}) Intervening contour based-Bias Ncut. 73

5.1 Average performance measures for cardiac sequences, for the proposed approach (New), the Euclidean radial basis approach, and the level set method. 89

Chapter 1

Introduction

Biomedical image segmentation is becoming one of the most fundamental roles in diagnosis and treatment of diseases as the new medical imaging technologies progress. Segmented images are nowadays used routinely in a wide range of applications, including localization of pathology, diagnosis, treatment planning, computer-integrated surgery, study of anatomical structure among others. However, medical segmentation is still challenging due to limited image contrast, presence of noise and variations in anatomy and pathology. To alleviate these issues prior knowledge is usually integrated into the segmentation method giving more robust results. In general, due to the specificity of the prior, numerous methods have been developed to solve specific cases. We will review some of the methods used in medical segmentation including model-free segmentation techniques, deformable models, graph cuts, atlas-based segmentation and convex optimization and explain the pros and cons of every approach.

The main objective of this work, is to segment the myocardium in short axis cardiac MR images. Segmentation of the myocardium provides valuable information for diagnosis and treatment in cardiac pathologies. From the segmentation, we can measure the ventricular volume, ejection fraction, wall thickening, wall motion and myocardium mass whose information can help in the diagnosis of myocardial hypertrophy, myocardial infarction and ventricular arrhythmias among others. But the detection of the myocardium is very challenging because of the signal loss, the presence of papillary muscles and that the borders are in contact with other organs that

have similar intensities. Therefore, a lot of algorithms have been implemented to solve these issues but the problem still remains open. For this purpose, we have presented two novel methods for cardiac segmentation. Although, these novel techniques were successfully applied to the cardiac data, they can be used to segment other type of biomedical images and natural images as it will be shown in the experimental validation.

The first technique proposed is based on normalized cuts which is an efficient graph theoretic segmentation method. Due to the difficulty and limitation to add prior knowledge to normalized cuts, it has not been widely used in medical segmentation. However, there are some techniques to incorporate prior knowledge into normalized cuts but they are still limited. We present a novel method to integrate shape prior knowledge into normalized cuts where the prior is included into the cost function without the inclusion of hard constraints and it can be extended easily to deal with multiple priors applying Principal Component Analysis (PCA). We conduct experiments using phantom data and MRI cardiac images as well as natural images for people segmentation from a public database and compare it with other normalized cut based segmentation algorithms. We demonstrate that our method gives promising results and can still give a good segmentation even when the prior is not accurate.

The second technique introduced is a new framework for image segmentation with statistical shape model enhanced level sets represented as a linear combination of non-Euclidean radial basis functions (RBFs). The shape prior for the level set is represented as a probabilistic map created from the training data and registered with the target image. The new framework has the following advantages: 1) the explicit RBF representation of the level set allows the level set evolution to be represented as ordinary differential equations and reinitialization is no longer required. 2) The non-Euclidean distance RBFs makes it possible to incorporate image information into the basis functions, which results in more accurate and topologically more flexible solutions. Experimental results are presented to demonstrate the advantages of the method, as well as critical analysis of level sets versus the combination of both methods.

1.1 Thesis Outline

The organization of this thesis is defined as follows: In the following chapter, we review the state-of-the-art on segmentation algorithms widely used in biomedical images. In Chapter 3, shape model techniques are described including methods for data alignment and for obtaining the shape variations such as Principal Component Analysis (PCA) among others. In Chapter 4, a novel technique is proposed using Normalized cuts with priors. In Chapter 5, we present a new framework using Level Sets based on Non-Euclidean Basis Functions with Statistical Shape Prior. Finally we end up with a conclusion.

1.2 Description of Short-axis MR Images

The heart is the organ that supplies blood and oxygen to all parts of the body. It is located in the chest cavity just posterior to the breastbone, between the lungs and above the diaphragm [1]. It is surrounded by a double-layered membrane called the pericardium. The wall of the heart consists of three distinct layers (Figure 1-1) [2]:

1. Epicardium (outer layer): It is the thin, transparent outer layer of the heart wall and is composed of delicate connective tissue. It is also considered the inner layer of the pericardium also known as the visceral layer.

2. Myocardium (middle layer): The myocardium, which is composed of cardiac muscle tissue, makes up the majority of the heart wall and is responsible for its pumping action.

3. Endocardium (inner layer): It is a thin layer of endothelium overlying a thin layer of connective tissue. It provides a smooth lining for the chambers of the heart and covers the valves.

The short axis view of the heart is the plane oriented perpendicular to the long (apex-base) axis which aligns the apex and the base of the heart. The short axis view shows an excellent cross sectional view of the right and left ventricles. The data

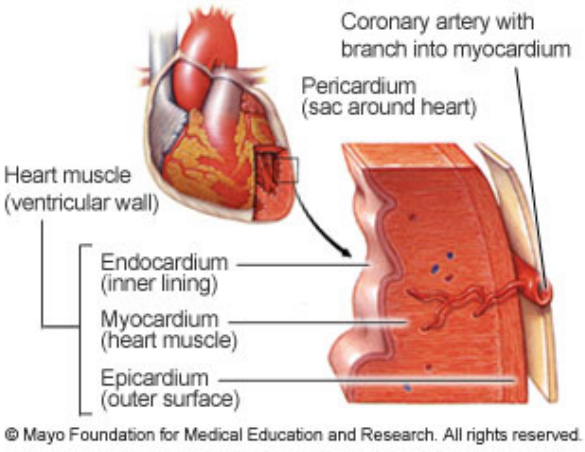

Figure 1-1: The heart wall is divided into three layers: epicardium, myocardium, and endocardium.

provided to run our experiments was performed on a Siemens Sonata 1.5T scanner (Siemens Medical Solutions, Erlangen, Germany) and three slices (8 mm thickness) in short axis view (basal, mid-ventricular, and apical) were acquired in all measurements (Figure 1-2) throughout the cardiac cycle. The pixel size was 1.3 x 1.3 mm (96 x 256 matrix interpolated to 192 x 256).

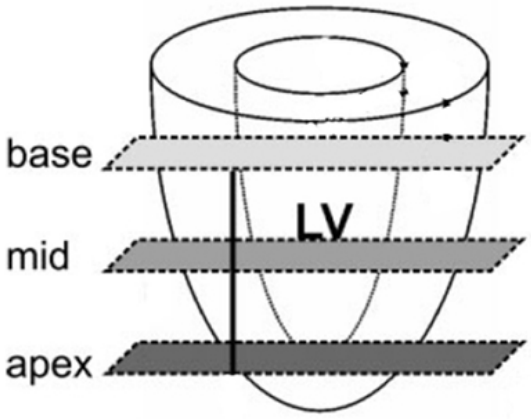

Figure 1-2: Three slices in short axis view were acquired: basal, mid-ventricular, and apical. (Author: Bernd Jung)

1.3 Issues in Cardiac MR Image Segmentation

Segmentation of the heart for short-axis MR images consists in delineating the outer wall, also called epicardium and the inner wall, known as endocardium. An example of the data is shown in Figure 1-3.

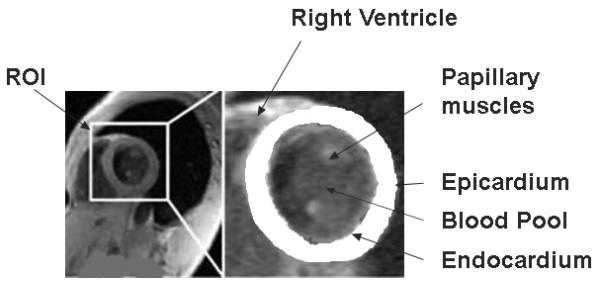

Figure 1-3: Cardiac MR image: the Region Of Interest (ROI) is obtained to get the segmentation of the myocardium (white) located between the epicardium and the endocardium. (Author: Bernd Jung)

As we can observe in Figure 1-3, each contour to be delineated presents specific segmentation difficulties [3]:

1. Epicardium: The epicardial wall is at the boundary between the myocardium and surrounding tissues, which show poor contrast with the myocardium. Segmentation of the epicardial wall is thus challenging, especially for the reduced thickness of the right ventricle.

2. Myocardium: Endocardium surrounds the left ventricle cavity. MRI provides quite good contrast between myocardium and the blood pool. But still segmentation difficulties exist, mostly originated from gray level inhomogeneities in the blood pool, and particularly because of the presence of papillary muscles and trabeculations (wall irregularities) inside the heart chambers, which have similar brightness levels to the myocardium. According to clinical standards, papillary muscles and trabeculae structures should be excluded from the endocardial wall segmentation.

3. Position along the apex-base axis: Segmentation complexity also depends on the slice level of the image. Mid-ventricular images are easier to segment than

apical and basal slice images (Figure 1-4). Indeed, MRI resolution is not high enough to resolve the size of small structures at the apex axis. In addition, ventricle shapes are strongly modified close to the base of the heart, because of the vicinity of the atria.

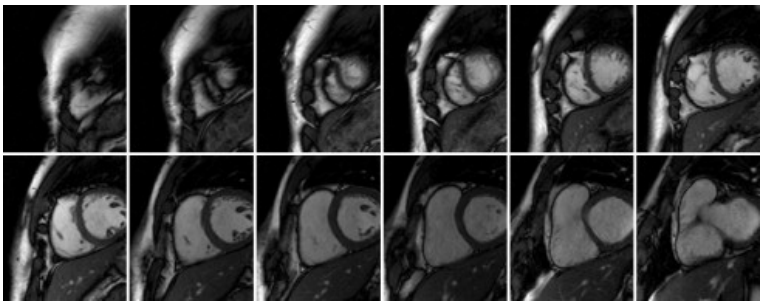

Figure 1-4: Cardiac images corresponding to 12 short-axis slices from apex to base. (Author: Petitjean)

Chapter 2

Review of Segmentation Methods

2.1 Introduction

In this chapter, we will review the state of the art of medical image segmentation including model-free segmentation techniques, deformable models, graph cuts, atlas-based segmentation and convex optimization. Model-free segmentation methods are traditional methods which rely on the intensity values of the image. Deformable models describe a group of computer algorithms that provide an abstract model of an object class by modelling the variability in shape, texture or imaging conditions in a certain class of objects [4]. This group includes snakes, level sets and active shape model approaches. Graph cuts is a general graph-based image segmentation which represents the image as a graph and seeks the minimum partition of that graph resulting in the segmentation of the image. Atlas based approach describes the anatomical structures in an atlas and the segmentation is given by a sort of alignment of that atlas to the target image. Convex optimization techniques allow to cast computer vision problems in terms of convex functionals. As a consequence, one can compute globally optimal solutions (or solutions with bounded optimality) that are independent of the initialization [5].

2.2 Model-free Segmentation

Model-free segmentation techniques are traditional methods of segmentation such as thresholding, region growing, and watershed. The segmentation is given according to the pixel intensities that reflect distinct tissue groups. These techniques are algorithmically motivated and there is not an energy model that leads to an optimization problem. The main methods of this group are the following [6]:

Thresholding: The most common one in this group is thresholding based on the idea that the image is constituted in dark and bright regions which represent the background and foreground. Then, pixels above certain threshold are considered as a foreground and pixels below or equal to that threshold are considered as a background. The key point of this approach is to find that threshold. It can be generalized to N regions by introducing $N-1$ thresholds. Thresholding algorithms can be categorized into global or local thresholding. If the threshold is applied to the entire image, the algorithm is a global thresholding algorithm. Otherwise, if the threshold depends on local properties of some regions, it is a local thresholding algorithm. The main problems of this method are that objects are often not separable using a threshold and the spatial context is ignored.

Region Growing: Region growing is a procedure that groups pixels or subregions into larger regions based on predefined similarity criteria such as intensity, texture and color properties. Region growing algorithm starts with a set of seed points. From these seed points, region growing algorithm grows regions by appending to each seed its neighboring pixels that have similar properties as the seed, according to the predefined similarity criteria. Similarity criteria may be difficult to define especially for medical images with low contrast. Moreover, if the similarity criterion is not properly defined, the regions may leak out and merge with other regions that belong to different anatomical parts. Region growing can also be sensitive to noise, causing extracted regions to have holes or even become disconnected, resulting in over-segmentation.

Watershed: It visualizes an image in three dimensions where the height of each

point represents its gradient value. The gradient value is interpreted as the altitude of a topographic relief. Then, morphological operations are applied just like pouring water into punctures of the topographic relief. When water from different punctures is starting to mix, a dam is built to stop the mixing. These dams are the boundaries of objects in the image. This approach is sensitive to noise. It may also cause over-segmentation. Therefore, the watershed algorithm is usually followed by a post-processing step to merge the separated regions that belong to the same anatomical part. Moreover, it is poor at detecting thin structures and structures with low signal-to-noise ratio [7].

2.3 Snakes

A snake or active contour [8], introduced by Kass et al. (1988), is an elastic band placed on an image which evolves by means of energy minimization to delineate an object of interest. To do so, the snake is first initialized near the object boundary. Then, the snake evolves towards the salient contour. When the snake has reached the object boundary, we say that the snake evolution has converged and hence it ceases the evolution. An example is shown in Fig. 2-1.

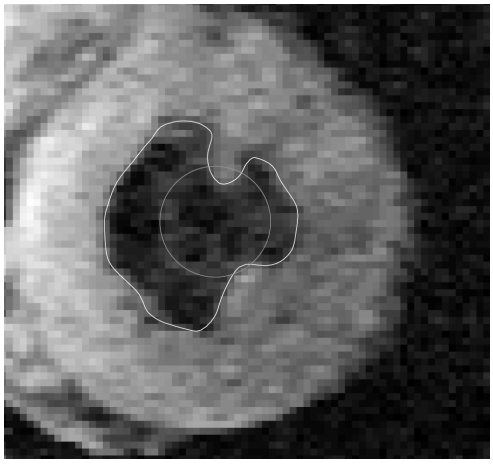

Figure 2-1: Segmentation of the left ventricle using snakes. The initial contour is plotted in grey and the final converged result is plotted in white. (Author: Chenyang Xu et al.)

Mathematically, this framework attempts to minimize an energy composed by the

sum of an internal and external energy:

- The external energy guides the snake towards the features of the image. Some of the common external terms are: $E_I = \pm\gamma I(C(s))$ which attracts the curve to high (or low) intensity points, $E_G = -\delta|\nabla(G(C(s)) * I(C(s)))|$ which attracts the curve to points with a large gradient and $E_E = -\zeta e^{-d(C(s))^2}$ which makes the contour to move near points in the edge map. $C(s) = (x(s), y(s))$ is a parametric contour or the contour of the snake and s is the parameter of the curve. In the last expression, $d(C(s))$ is the distance to the closest boundary point and $G(C(s)) * I(C(s))$ denotes the image convolved with a Gaussian smoothing filter [9].

- The internal energy tries to preserve the smoothness in the shape of the curve. The stretching and the bending energies are called internal energies which are proportional to the first and second derivative of the curve respectively. The stretching term penalizes the length of the contour whereas the bending term penalizes the total curvature of the contour. The total internal energy of the snake can be defined as $E_{int} = E_{stretch} + E_{bending}$.

The external and internal energies combined together prefer a compromise of a short contour which captures as much image gradient as possible. The final solution given by the snake is the one which minimizes the sum of the external and internal energies as follows:

$$E(C(s)) = \underbrace{\int_0^1 E_{ext}(C(s))ds}_{External\ Energy} + \underbrace{\underbrace{\alpha \int_0^1 |C_s(s))|^2 ds}_{E_{stretch}} + \underbrace{\beta \int_0^1 |C_{ss}(s))|^2 ds}_{E_{bending}}}_{Internal\ Energy} \tag{2.1}$$

where $C : [0, 1] \rightarrow \Omega$ is a parametric contour, α and β control the smoothness of the curve and C_s and C_{ss} are the first and second derivative of the contour respectively.

To minimize the energy functional, we apply an optimization tool known as calculus of variations [10] to take a derivative with respect to a function. After taking

the functional derivative equate the derivative to zero to find the minimum. The resulting Euler-Lagrange equation is:

$$\frac{dE}{dC} = \frac{dL}{dC} - \frac{d}{ds}\frac{dL}{dC_s} + \frac{d^2}{(ds)^2}\frac{dL}{dC_{ss}} = -\nabla E_{ext} - \alpha C_{ss} + \beta C_{ssss} = 0 \tag{2.2}$$

There are several numerical techniques to solve the Euler equation using optimization techniques such as gradient descent or dynamic programming [11] and discretization methods such as finite differences [8] or finite elements [12]. We apply first gradient descent to solve the equation. To do so, the parametric contour C is converted into a function of time and equated to the partial derivative of C to time instead of 0. The reason for this can be seen if one assumes that, after a long time when the snake has converged to a minimum, its derivative to time will be zero, and hence the Equation 2.2 is satisfied. For simplicity, we call the external force ∇E_{ext} as F_{ext} and the gradient descent rule becomes:

$$\frac{\partial C(s)}{\partial \tau} = -\frac{dE}{dC} = F_{ext} + \alpha C_{ss}(s,\tau) - \beta C_{ssss}(s,\tau) = 0 \tag{2.3}$$

This equation can be interpreted as force balance that drives the snake. The internal force (the stretching and the bending terms) and the external force (terms involving image gradients) are trying to balance each other. When the net result force is zero, the snake stops evolving, and we obtain a local minimum [13].

To represent the snake, we need a polygonal representation of the continuous contour. This is performed by separating C into its two components X and Y and $Fext$ into f_x and f_y and then by representing the continuous parameter $s \in [0,1]$ with indices $i \in \{0,1,,n-1\}$, with n being the total number of points. The finite difference approximation is used to approximate the spatial derivatives: $x_{ss} = X^{\tau}_{i+1} - 2X^{\tau}_{i} + X^{\tau}_{i-1}$ and $x_{ssss} = X^{\tau}_{i+2} - 4X^{\tau}_{i+1} + 6X^{\tau}_{i} - 4X^{\tau}_{i-1} + X^{\tau}_{i-2}$. The resulting discrete equations are:

$$\frac{X_i^{\tau+1} - X_i^{\tau}}{\zeta} = \alpha(X^{\tau}_{i+1} - 2X^{\tau}_{i} + X^{\tau}_{i-1}) - \beta(X^{\tau}_{i+2} - 4X^{\tau}_{i+1} + 6X^{\tau}_{i} - 4X^{\tau}_{i-1} + X^{\tau}_{i-2}) + f_x(X^{\tau}_{i}, Y^{\tau}_{i}) \tag{2.4}$$

$$\frac{Y_i^{\tau+1} - Y_i^{\tau}}{\zeta} = \alpha(Y_{i+1}^{\tau} - 2Y_i^{\tau} + Y_{i-1}^{\tau}) - \beta(Y_{i+2}^{\tau} - 4Y_{i+1}^{\tau} + 6Y_i^{\tau} - 4Y_{i-1}^{\tau} + Y_{i-2}^{\tau}) + f_y(X_i^{\tau}, , Y_i^{\tau}) \tag{2.5}$$

where τ represents an instant time and ζ the step length [13]. In matrix form Equations 2.4 and 2.5 become:

$$\frac{X^{\tau+1} - X^{\tau}}{\zeta} = -A_x^{\tau} + f_x^{\tau} \tag{2.6}$$

$$\frac{Y^{\tau+1} - Y^{\tau}}{\zeta} = -A_y^{\tau} + f_y^{\tau} \tag{2.7}$$

where $f_x = \frac{\partial F_{ext}}{\partial x}$, $f_y = \frac{\partial F_{ext}}{\partial y}$, A is a pentadiagonal banded matrix (cyclic if curve is closed) and X and Y are the components of C which are a vector with x-values and y-values respectively of coordinates of points along the curve.

The matrix A is a pentadiagonal banded matrix with size $n \times n$ with n being the number of vertices:

$$A = \begin{pmatrix} c & b & a & & & & a & b \\ b & c & b & a & & & & a \\ a & b & c & b & a & & & \\ & \ddots & \ddots & \ddots & \ddots & \ddots & & \\ & & & a & b & c & b & a \\ a & & & & a & b & c & b \\ b & a & & & & a & b & c \end{pmatrix}$$

where $a = \beta$, $b = -(4\beta + \alpha)$ and $c = 6\beta + 2\alpha$.

The numerical stability of Equations 2.6 and 2.7 depends on the time step ζ. For practical time step values, they may be unstable [13]. Instead, a semi-implicit procedure [14] is followed by rewriting them as:

$$\frac{X^{\tau+1} - X^{\tau}}{\delta\tau} = -A_x^{\tau+1} + f_x^{\tau} \tag{2.8}$$

$$\frac{Y^{\tau+1} - Y^{\tau}}{\delta\tau} = -A_y^{\tau+1} + f_y^{\tau} \tag{2.9}$$

Then, the final solution becomes [13]:

$$x^{\tau+1} = (I_n - \zeta A)^{-1}(x^{\tau} + \zeta f_x^{\tau}) \tag{2.10}$$

$$y^{\tau+1} = (I_n - \zeta A)^{-1}(y^{\tau} + \zeta f_y^{\tau}) \tag{2.11}$$

where I_n is the $n \times n$ identity matrix.

The most interesting feature of snakes is their closed shape even if there is noise. The limitations of the method are high sensitivity to initialization, fixed topology, local minima and the difficulty to work with noisy images or with lack of contrast data. Moreover, it has also difficulties in progressing into boundary concavities. Other implementations have been proposed in order to improve the performance of the standard snakes. For example, Cohen et al. suggested a balloon based pressure force to enlarge the capture range of snakes [12]. The balloon model allows to pass over weak borders and stop on salient edges. It also reduces the sensitivity to initialization. However, this model may not move into boundary concavities or may overwhelm weak boundaries. Xu et al. proposed a Gradient Vector Flow snake (GVF) [15] where instead of directly using image gradients as an external force, they use a spatial diffusion of the gradient of an edge map of the image. It was proposed to deal with the sensitivity to initialization and inability to move into boundary concavities. In spite of its numerous advantages, this method is still susceptible to local minima in some images since it is based on local measurements such as image gradients, it is sensitive to parameters and the calculation of the gradient vector field can be computationally expensive.

Moreover, some works were suggested to deal with the difficulty of the topological adaptation such as splitting or merging model parts, a useful property for recovering multiple objects or objects with unknown topology [16], however they require sophisticated schemes [17, 18, 19]. Novel geometric models of active contours were proposed

by Caselles et al. [20]. These models are based on the theory of curve evolution and geometric flows where the curve is propagating by means of velocity which contains a term to regulate the curve and another to shrink or expand it towards the boundary. The model is given by a curve evolution approach and not an energy minimization. It allows automatic changes in topology when this model is implemented with level sets-based numerical algorithms whose technique is described in detail in Section 2.4. Thereby, several objects can be detected simultaneously without adding complexity or prior knowledge.

2.4 Level Sets

Snakes also referred as active contours [8] control the deformation of an initial contour curve $C(p)$, $p \in [0,1]$ according to internal and external forces achieving a minimum energy configuration at high-gradient regions of the image as described in Section 2.3. This model is usually implemented with a parametric framework in which the deformable model is explicitly represented in its parametric form and defined on a regular spatial grid, tracking its point positions in a Lagrangian formulation [16]. A limitation of parametric active contours is that is challenging to change the topology of the evolving contour. An alternative representation for such closed contours is to use a level set representation. The level set technique, introduced by Osher and Sethian [21] in 1988, is based on an evolving surface in a higher dimensional space represented as a signed distance function ϕ as shown in Fig. 2-2.

A boundary C is thus represented as the zero level set of higher dimension ϕ, satisfying:

$$\begin{cases} \phi(x,y,t) > 0, \ for (x,y) \in \Omega_{in}(t), \\ \phi(x,y,t) < 0, \ for (x,y) \in \Omega_{out}(t), \\ \phi(x,y,t) = 0, \ for (x,y) \in \partial\Omega_{in}(t) = C(t) \end{cases}$$

where Ω_{in} is the region bounded by C and Ω_{out} is defined as $\Omega_{out} = \Omega \backslash \Omega_{in}$.

In order to derive an equation of motion for this level set function ϕ, we assume that an initial curve C is embedded as the zero level set of a higher dimension function:

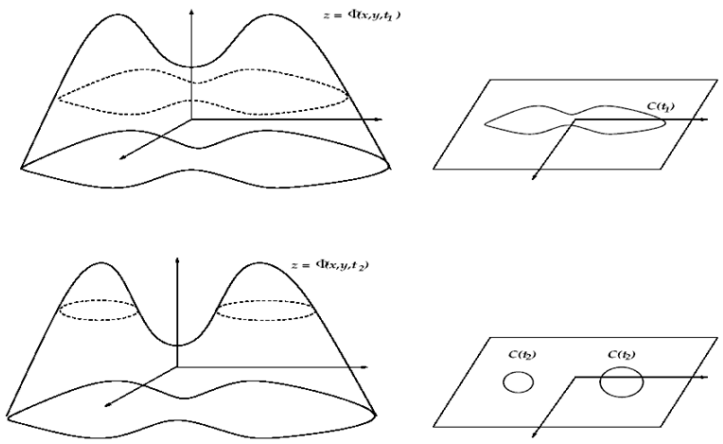

Figure 2-2: Level set methodology and curve propagation. The left column shows the evolving level set function, while, on the right, the corresponding curve that is the zero level set values of the surface is illustrated. (Author: Nikos Paragios et al.)

$C_0 = \{(x, y) \backslash \phi(x, y, 0) = 0\}$. At any time t, the front is given by the zero level set of the time-dependent level set function ϕ:

$$\phi(x, y, t) = 0 \tag{2.12}$$

where $\phi(x, y, t)$ is the height of the surface at the position (x, y) and time t. This zero level set can represent the set of evolving contours which are able to split and merge to delineate certain object boundaries.

To obtain the evolution equation, we differentiate $\phi(x, y, t)$ with respect to time using the chain rule [13]:

$$\frac{d\phi(x, y, t)}{dt} = \frac{\partial\phi(x, y, t)}{\partial t} + \nabla\phi(x, y, t) \cdot (x_t, y_t) \tag{2.13}$$

where (x_t, y_t) is the velocity at point (x, y) on the geometric contour. We take this partial derivative and set it to zero to achieve an Euler-Lagrange equation:

$$\frac{\partial\phi(x, y, t)}{\partial t} + \nabla\phi(x, y, t) \cdot (x_t, y_t) = 0 \tag{2.14}$$

Assuming that the surface moves in the normal direction to the surface, we take the velocity (x_t, y_t) and constrain motion in the normal direction. Thereby, we can

define the speed of the surface as:

$$F = (x_t, y_t) \cdot n \tag{2.15}$$

for unit normal n with $n = \frac{\nabla\phi(x,y,t)}{|\nabla\phi(x,y,t)|}$ on the surface $\phi(x, y, t)$. Combining the unit normal n with Equation 2.15, and Equation 2.14, we obtain the classical level set equation introduced by Osher and Sethian [21]:

$$\phi_t + F|\nabla\phi(x, y, t)| = 0, \tag{2.16}$$

where $\phi_t = \frac{\partial\phi(x,y,t)}{\partial t}$ and the function F initially was expressed by Osher as $F = div\left(\frac{\nabla\phi}{|\nabla\phi|}\right)$ but since then, many other forces were suggested.

Typically, after an initialization we can evolve $\phi(x, y, t)$ by updating each $\phi(x, y, t)$ for each (x, y) position at time t. Alternatively, we can use a narrow band technique [22] to update just a band around the zero level set contour [13].

Since its introduction, the concept of deformable models for image segmentation defined in a level set framework has motivated the development of several families of methods such as: geometric active contours based on mean curvature flow, gradient-based implicit active contours and geodesic active contours [16]. Geometric active contours were introduced by Caselles et al. [20] by adding a constant inflation force term and multiplying the force by a term inversely proportional to the smooth gradient of the image. In this context the model is forced to inflate on smooth areas and to stop at high gradient locations [16]. Malladi, Sethian and Vemuri [23] presented a gradient-based speed function for the general Hamilton-Jacobi equation of motion in Equation 2.16. The authors decompose the speed term into two components V_a and V_G which are the advection term independent of the geometry and a remainder term which depends on the front geometry, respectively. The front propagation stops at high-gradient location depending on the value V_G [16]. Geodesic active contours, introduced simultaneously by Kichenassamy et al. [24] and Caselles et al. [25], connect classical snakes based on energy minimization and geometric active contours based on the theory of the curve evolution. The model is derived from energy-based

snakes and performs the extraction of the contour via the calculation of geodesics.

The major problem of boundary-based level set segmentation methods is related to boundary leakage through weak or missing boundary parts. The second issue is that the segmentation process is very sensitive to the initialization of the level set function as the model is prone to converge to false edges that correspond to local minima of the energy functional. Medical images generally suffer from insufficient and false edges caused by acquisition artifacts and machine noise from different modalities. Two approaches can be followed to address these limitations [16]. The first approach is to fuse regularizer terms based on clustering, bayes, shape and couple-surfaces in the speed function [26]. A second approach is to reformulate the problem in terms of region-based segmentation techniques derived from the Mumford-Shah functional implemented with level sets-based numerical algorithms.

Region-based active contours were derived from the Mumford-Shah segmentation framework, which was initially proposed in [27]. The authors presented a new segmentation framework by minimizing an energy functional involving a piecewise smooth representation of an image as follows:

$$E(S,f) = \alpha \int_{\Omega} (f-I)^2 dx + \beta \int_{\Omega \setminus S} |\nabla f| dx + H^{n-1}(S) \tag{2.17}$$

where H^{n-1} is the $(n-1)$ dimensional Hausdorff measure and (α, β) are positive real parameters. In this energy functional, the first term ensures that is a good approximation of the original image I, the second term ensures the smoothness of f and the last term penalizes the length of the set of contours. This type of region-based segmentation method relies on the homogeneity of the object to segment. Based on the Mumford-Shah segmentation framework, Chan and Vese [28] introduced the following homogeneity-based functional which aims at partitioning an image into regions with piecewise constant intensity:

$$E(C) = \lambda_0 \int_{insideC} |I-\mu_{in}|^2 d\Omega + \lambda_1 \int_{outsideC} |I-\mu_{out}|^2 d\Omega + \gamma_1 length(C) + \nu_2 Area(C) \tag{2.18}$$

where I is the original image, μ_{in} and μ_{out} are the average values of pixels inside and outside the curve C respectively, and the last two terms are regularizer terms that put constraints on the length and the area of the curve. In a level set framework, Equation 2.18 becomes:

$$E(C) = \lambda_0 \int_{insideC} |I-\mu_{in}|^2 H(\phi) d\Omega + \lambda_1 \int_{outsideC} |I-\mu_{out}|^2 (1-H(\phi)) d\Omega + \gamma_1 length(C) + \nu_2 Area(C) \tag{2.19}$$

where H is the Heaviside function. Advantages of this method include the possibility of segmenting objects with weak edges and robustness to initialization, avoiding the problem of local minima at spurious edge locations or leakage of the model at missing boundary parts [16].

In parallel effort, Tsai, Yezzi et al. [29] presented a reformulation of the Mumford-Shah energy functional using a gradient flow formulation and a level set framework from a curve evolution perspective [16].

2.5 Active Shape Models

Active Shape Models (ASM) is a statistical shape model built up from a hand segmented training data. Let a contour be represented as a set of ordered sequence of points, i.e., $x = [X_0, Y_0, X_1, Y_1, ..., X_{n-1}, Y_{n-1}]$. Thus, when we refer to a distribution of shapes, essentially, we are referring to the distributions of random vectors x. ASM assumes that the distribution of x is a multivariate Gaussian [13]:

$$x \sim \frac{1}{\sqrt{(2\pi)^{2n}|\Sigma|}} exp\left(-\frac{1}{2}(x-\mu)^T \Sigma^{-1}(x-\mu)\right) \tag{2.20}$$

where μ and Σ are, respectively, the mean vector and the $2n \times 2n$ covariance matrix for the shape x, n is the number of shape points and $|\ |$ denotes a determinant. In principle, one can estimate the mean vector and the covariance matrix from the training samples. Once these parameters are estimated, we can proceed to perform the Bayesian inference for an unknown test image. But there is a potential problem

with this approach. The estimation of the covariance can be adversely affected when there is a small number of training examples compared to the number of shape points such that the covariance matrix becomes singular, making the inference extremely difficult.

To deal with this problem, ASM represents the multivariate joint Gaussian distribution in Equation 2.20 into a product of $2n$ univariate Gaussians. As Σ is real, symmetric and positive definite by singular value decomposition can be written as $\Sigma = UDU^T$ where U is a $2n \times 2n$ orthogonal matrix and D is a $2n \times 2n$ diagonal matrix such as $D = diag(\sigma_1^2, \sigma_2^2, ..., \sigma_{2n}^2)$. The determinant of the covariance matrix is now $|\Sigma| = |U||D||U^T| = \prod_{i=1}^{2n} \sigma_i^2$. Moreover, ASM ignores the Gaussian distributions with small variances by retaining m larger variances because a univariate Gaussian with a small variance can affect adversely the entire joint multivariate Gaussian distribution. Taking into account these algebraic facts the Equation 2.20 becomes [13]:

$$\frac{1}{\sqrt{(2\pi)^m|\Sigma|}} exp\left(-\frac{1}{2}(x-\mu)^T\Sigma^{-1}(x-\mu)\right) = \prod_{i=1}^{m} \frac{1}{\sqrt{2\pi}\sigma_i} exp\left(-\frac{(u_i^T(x-\mu))^2}{2\sigma_i^2}\right) \tag{2.21}$$

with $\Sigma = [u_1...u_m]diag(\sigma_1^2, ..., \sigma_m^2)[u_1...u_m]^T$.

Now, to sample a random shape we only need m random numbers $v_1, v_2, ..., v_m$ from zero-mean univariate Gaussians with variances $\sigma_1^2, \sigma_2^2, ..., \sigma_m^2$. The other $2n - m$ random numbers are all zeros. Then, we would obtain the shape x by solving the following sets of linear equations:

$$u_i^T(x-\mu) = v_i, i = 1, 2, ..., m$$
$$u_i^T(x-\mu) = 0, i = m+1, ..., 2n$$

The solution is given by:

$$x = \mu + U[v_1, v_2...v_m 0...0]^T = \mu + \sum_{i=1}^{m} v_i u_i \tag{2.22}$$

To train the ASM, first the N training shapes must be aligned with each other.

After the alignment, the next step is to compute the mean and the covariance of the training data [30]:

$$\mu = \frac{1}{N}\sum_{j=1}^{N} x_j$$
$$\Sigma = \frac{1}{N}\sum_{j=1}^{N}(x_j - \mu)(x_j - \mu)^T$$

Finally, the eigenvectors u and eigenvalues λ of the covariance matrix Σ are computed and a value for m is chosen, i.e., how many eigenvectors need to be kept for describing ASM [13]. The following formulation can then approximate any of the training set x:

$$x \sim \mu + Uv$$
$$v = U^T(x - \mu)$$

where $U = (u_1|u_2|...|u_t)$ contains the m eigenvectors of the covariance matrix and v defines a set of parameters of a deformable model. By varying the elements of v we can vary the shape x. Therefore, a new shape is described by the average shape vector and a linear combination of eigenvectors of the variations around the average shape as shown in Fig. 2-3. The eigenvectors define a rotated coordinate frame and the vector v defines points in this rotated frame. Suitable limits for the shape parameters may be established to ensure that the shape generated is similar to those in the original training set, for example $-3\sqrt{\lambda_k} \leq v_k \leq 3\sqrt{\lambda_k}$ where λ_k is the corresponding eigenvalue.

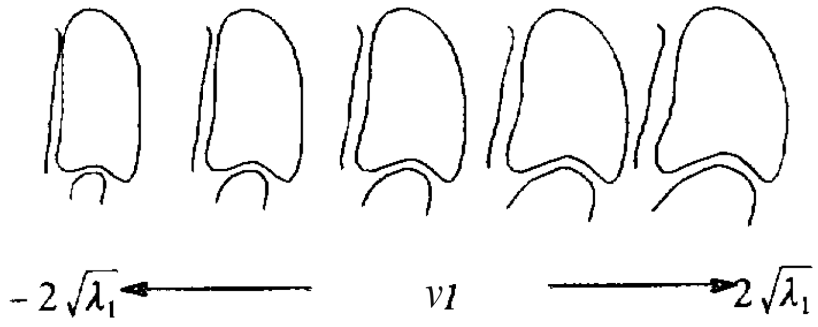

Figure 2-3: Effect of varying the first shape parameter around the average shape. (Author: T. F. Cootes)

ASM can also be formulated as a minimization of a cost function described in detail in [13] or using affine transformations to fit the shape model to new data sets by Cootes et al. [30]. The latter work may be more suitable where large transformations such scaling or rotations are desired.

The ASM performance can be significantly improved using a multi-resolution implementation, in which the search is guided by a coarse level of a gaussian image pyramid, and is progressively refined [30]. This leads to much faster, more accurate and more robust search.

Active Appearance models (AAM) are an extension of active shape models whose main difference is that in addition to the shape variability, the texture variation is also incorporated to the model. A novel multistage hybrid appearance model methodology is presented in [31] which combines the strengths of ASM that finds local structures fairly well to the strengths of AAM which is optimized on global appearance but it is less sensitive to local structures and boundary information. The main issues of these two methods are that the creation of a training set is a tedious and time-consuming task and that the accuracy of the segmentation relies in the variability of the training data set.

2.6 Graph Cuts

It is a graph based image segmentation which represents the image as a graph and the final segmentation is the result of finding the minimum cut of that graph. Graph cuts proved to be an useful multidimensional optimization tool which can enforce piecewise smoothness while preserving relevant sharp discontinuities [32].

First, we will introduce the basic terminology [32]. A graph $G = \langle V, \varepsilon \rangle$ is defined as a set of nodes V and a set of edges ε connecting neighbour nodes. The nodes set $V = P \cup \{s, t\}$ contains non-terminal nodes P which represent the pixels of the image and two additional special nodes known as terminal nodes which are called the source s, and the sink t. Each graph edge is assigned some nonnegative weight $w(p, q)$. An edge is called a t-link if it connects a non-terminal node in P with a terminal. An

edge is called a n-link if it connects two non-terminal nodes. The goal is to find the minimum cut through the graph that separates source and sink which is equivalent to assign the pixels to either source or sink. Any cut corresponds to some binary partitioning of an underlying image into object and background segments.

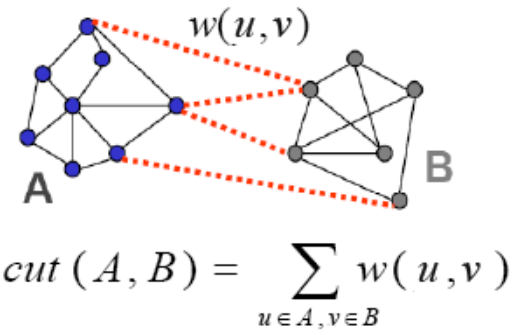

Figure 2-4: Example of graph-based image segmentation.

The optimal bipartitioning of a graph is the one that minimizes this cut value which corresponds to the optimal variable assignment for the nodes (Fig. 2-4):

$$cut(A, B) = \sum_{u \in A, v \in B} w(u, v) \tag{2.23}$$

where A and B are the partitions for background and foreground. Although there are an exponential number of such partitions, there exist efficient algorithms to solve this problem including max flow algorithms which have been successfully used for a wide variety of vision problems.

A standard form of the energy function for a binary pixel labeling problem is:

$$E(u_1, ..., u_n) = \sum_i D(u_i) + \sum_{i,j \in N} w_{ij} \delta(u_i \neq u_j) \tag{2.24}$$

where $u_1, ..., u_N$ are binary pixels to be determined with $u_i \in \{0, 1\}$, N is the total number of pixels in the image, $D(u_i)$ is the penalty to assign to a pixel u an intensity $\{0, 1\}$, for example $D_i(0) = (I_i - \mu_1)^2$ and $D_i(1) = (I_i - \mu_2)^2$ with μ being the mean, and δ is the identity function which is 1 if its argument is true and 0 otherwise. Typically this function δ imposes smoothness in the solution, for example it will

penalize if two neighboring pixels have different labels, and is weighted by a parameter w_{ij} to control the level of smoothness. Globally, the first term says that the variable assignment u should agree with the observed data, and the second term states that most nearby pixels should have the same intensity label [32].

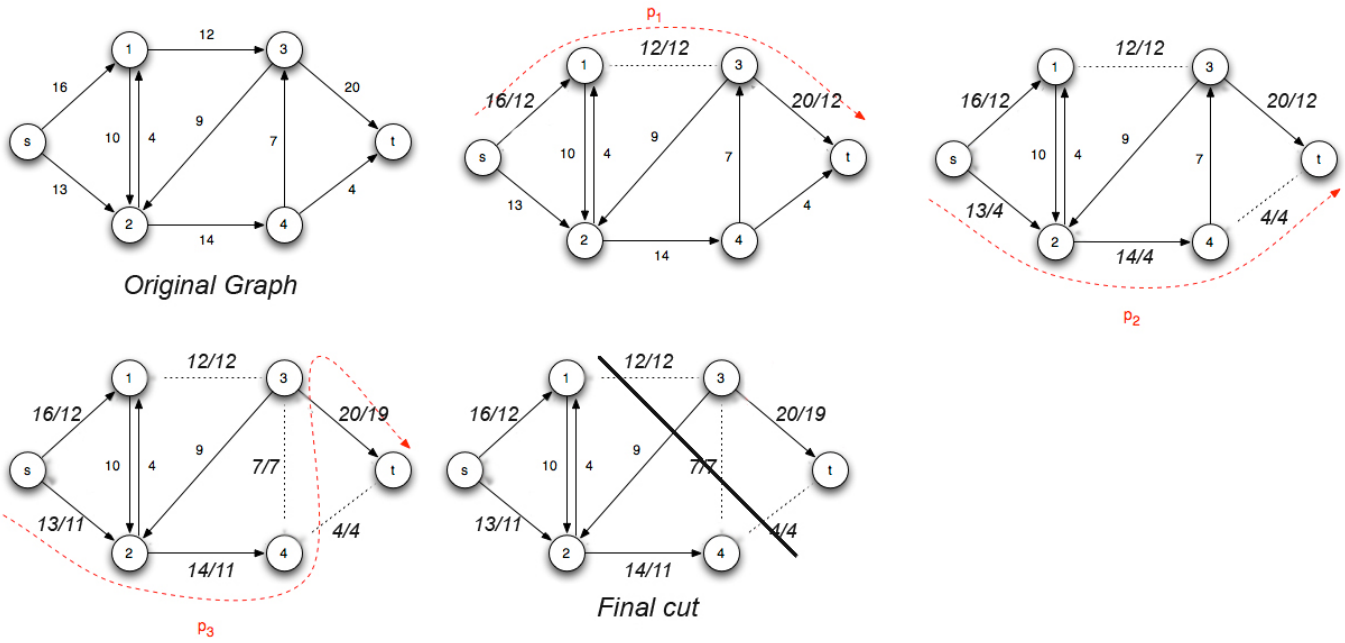

Figure 2-5: An example of the Ford-Fulkerson method.

According to the Ford-Fulkerson theorem, we can re-write the minimum cut problem as a maximum flow problem. Ford and Fulkerson also proposed a technique called the Ford-Fulkerson method which computes the maximum flow in a flow network. The idea behind the algorithm is simple. As long as there is a path from the source (start node) to the sink (end node), with available capacity on all edges in the path, we increase flow with the minimum residual capacity along this path. Then, we find another path until all paths have at least one edge with no available capacity.

The edges with no residual capacity represent the cut through the graph. An example is shown in Fig. 2-5. Efficient code is provided by Vladimir Kolmogorov with linear running time [33] in the average case. The global optima solution is guaranteed if the considered energy has only two labels (source and sink), the regional models are fixed i.e., the means of the two regions are known a priori, and the edges are

non-negative.

Some extensions to multilabel problems have been implemented including α-Expansion and $\alpha - \beta$ Swap whose idea is to try to break the multilabel task into a sequence of binary tasks [34]. The solution of those two approaches may not ensure global optimum.

2.7 Atlas-based Segmentation

In general, an atlas incorporates the locations and shapes of anatomical structures, and the spatial relationships between them [35]. It can be generated by manually segmenting an individual image or by integrating information from multiple segmented images, for example from different individual subjects. Given an atlas, an image can be segmented by mapping its coordinate space to that of the atlas according to some image quality criterion, a process commonly referred to as registration. Labeling an image by mapping it to an atlas is consequently known as atlas-based segmentation, or registration-based segmentation [35]. The idea behind is to align an atlas image to a target image to be segmented by some spatial transformation which maps the atlas image space onto the target image space. A coordinate transformation is estimated which maximizes the similarity of the target image and the deformed atlas. Once aligned, the label for each image voxel can be given by looking up the structure at the corresponding location in the atlas under the resulting coordinate mapping. The Fig. 2-6 illustrates an example of the basic process.

The correctness of a given transformation is typically quantified by a so-called similarity measure. A similarity measure that has been empirically found to be particularly well-suited for many registration applications is mutual information (MI) based on the information-theoretic entropy concept [35, 36]. Studholme et al. proposed normalized mutual information which has been found to be slightly more robust [37]. The are many implementations of both methods to estimate the image entropies including Parzen windowing [38] or the use of discrete 2d histograms [39].

Maximizing only the similarity criterion provides under-constrained equations,

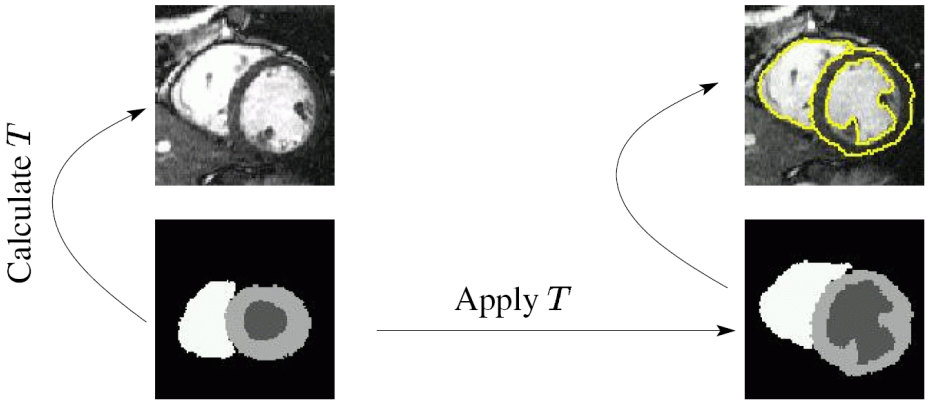

Figure 2-6: Registration of a cardiac atlas in form of a labelled image to a MR image of the heart. (Author: M. Lorenzo-Valdes)

that makes image registration an ill-posed problem and thus requires the use of additional constraints [3]. One way to deal with this issue, is to restrict the transformation space to parametric transformations [3], such as cubic splines [40] or the basis of eigenshapes, obtained with a PCA on the database of shapes [41]. Another way is to add a regularization term to the similarity criterion [3], such as a classical viscous fluid model [42], or a statistical model [41]. In this latter work, the shape variability is modeled with probabilistic shape models, including a probabilistic atlas, that provides the probability that a structure appears at each pixel.

2.8 Convex Optimization

Both parametric contours and implicit level set representations generally only find locally optimal solutions where the optimality is not guaranteed whereas recently developed convex relaxation schemes provide solutions which are either optimal or within a bound of the optimum [43].

The idea behind convex relaxation is that starting with a nonconvex problem, we first find an approximate, but convex, formulation of the problem. By solving this approximate problem, the exact solution to the approximate convex problem is obtained. This solution is then projected back to the original nonconvex problem [44]. An example is shown in Fig. 2-7.

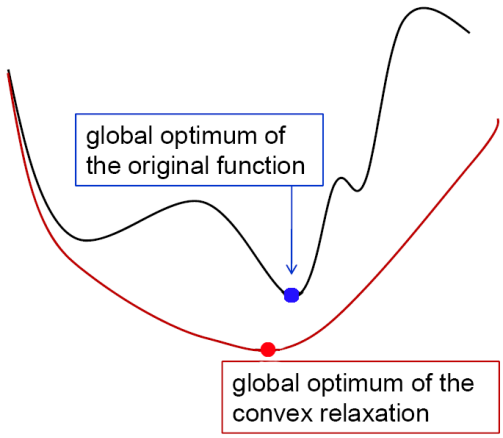

Figure 2-7: Approximation of a non-convex function in a convex one. (Author: Thomas Brox)

Many methods for global optimization require a cheaply computable lower bound on the optimal value of the nonconvex problem. Two standard methods for doing this are based on convex optimization [44]. In relaxation, each nonconvex constraint is replaced with a looser convex constraint. In Lagrangian relaxation, the Lagrangian dual problem is solved, which is complex. The solution to the dual problem provides a lower bound on the optimal value of the original nonconvex problem.

The backprojected solution may not be optimal as shown in Fig. 2-8 where u is the solution of the original problem and the relaxed problem results in w which is the global optima of the convex problem but when it is projected $\pi(w)$ to the original problem, the solution is not global optima anymore. The optimality bound is defined by $E(w) <= E(u) <= E(\pi(w))$.

We can use the following general equation to compute a segmentation of an image [43, 45]:

$$min_{\Omega_i} \left\{ \frac{1}{2} \sum_{i=0}^{k} Per(\Omega_i; \Omega) + \sum_{i=0}^{k} \int_{\Omega_i} f_i(x) dx \right\} \tag{2.25}$$

such that $\bigcup_{i=0}^{k} \Omega_i = \Omega, \Omega_s \bigcap \Omega_t = \emptyset \; \forall s \neq t$ with domain $\Omega \subset \mathbb{R}^d$. The minimization of Equation 2.25 will partitionate the domain Ω into $k+1$ pairwise disjoint sets Ω_i. The first term is the regularizer term which measures the perimeter of the set Ω_i which leads to smooth segmentation boundaries. The second term is the data term based

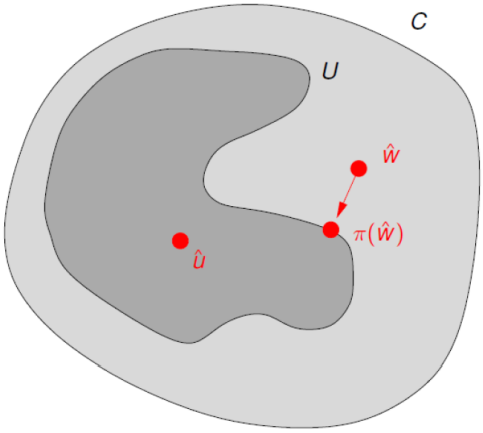

Figure 2-8: Process of convex optimization. u is the solution of the original problem and w the solution to the relaxed problem. The projected solution $\pi(w)$ to the original problem is not the global optimal solution of the original problem. (Author: Bastian Goldlucke)

on the features of the images. One example of data term is the piecewise constant Mumford-Shah functional where $f_i(x) = (I(x) - c_i)^2$ which is the squared difference of the input image I to some mean intensity c_i as described in Section 2.4.

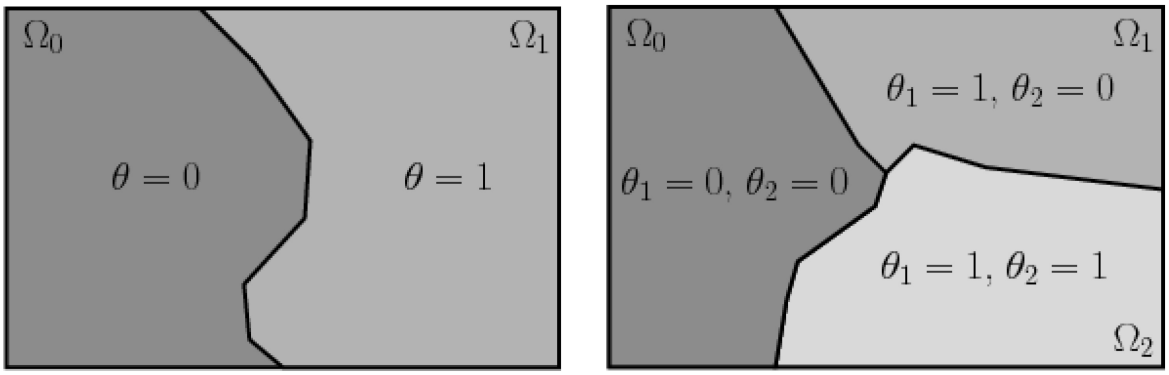

(a) (b)

Figure 2-9: (a) The two-label case: A binary function θ is used to partition the image domain Ω into two regions. (b) The three-label case: Two binary functions $\theta_1 \geq \theta_2$ are used to partition the image domain Ω into three regions. (Author: Cremers)

Firstly, we will review the functional convex representation for the binary problem case and extend it for the multi-label case [43, 45]. A binary function $\theta : \Omega \rightarrow \{0, 1\}$ is used to model the partition of the image domain into two regions such as $\theta(x) = 0 \ if \ x \in \Omega_0$ and $\theta(x) = 1 \ if \ x \ \in \Omega_1$. Fig. 2-9.a shows an example of partitioning the

image domain Ω into two regions with one binary function θ. The goal is to rewrite the Equation 2.25 in terms of the binary function θ. Starting for the two label case, the perimeter of the set Ω_1 is given by the weighted total variation of θ [43]:

$$Per(\Omega_1; \Omega) = \int |D\theta| \tag{2.26}$$

where $\int |D\theta|$ denotes the Total Variation of θ. For binary functions θ, it is equal to the total interface area. $D\theta$ is the distributional derivative of θ. For differentiable functions θ it is simply given by $D\theta = \nabla\theta dx$. To make the problem convex, θ is relaxed by allowing to vary smoothly in the interval $[0, 1]$.

There exists a more general formulation of the Total Variation [46, 47, 48]:

$$\int_\Omega |D\theta| = \sup_{\xi:|\xi(x)|\leq 1} \left\{ -\int_\Omega \theta \text{ div } \xi \text{ dx} \right\} \tag{2.27}$$

where $\xi = (\xi^1, ..., \xi^k)^T : \Omega \to \mathbb{R}^d$ is the dual variable and $|.|$ denotes the Euclidean vector norm. This formulation is also called the dual formulation of the Total Variation. The main advantage of the dual formulation over the original formulation is, that it is valid for any L_1 integrable function, but it comes along with inequality constraints on the dual variable ξ which brings some additional complexity to the formulation [45].

For the multiple label case, the $k+1$ regions Ω_i in Equation 2.25 are represented by a labeling function $u : \Omega \to \{0, ..., k\}$ where $u(x) = l$ if and only if $x \in \Omega_i$. One can equivalently represent this multilabel function by k binary functions $\theta(x) = (\theta_1(x), ..., \theta_k(x))$ defined by:

$$\theta_i(x) = \begin{cases} 1 \text{ if } u(x) \geq l \\ 0 \text{ otherwise} \end{cases} \tag{2.28}$$

representing its upper level sets [43]. In turn, the labeling function u can be recovered from these functions via the relation:

$$u(x) = \sum_{i=1}^{k} \theta_i(x) \tag{2.29}$$

An example is shown in Figure 2-9.b for $k = 2$ where two functions θ_1 and θ_2 are used to partition the image domain Ω into three regions. A one-to-one correspondence between multilabel functions $u(x)$ and vectors $\theta = (\theta_1, ..., \theta_k)$ of binary functions is guaranteed by constraining θ to the ordered set [45]:

$$B = \{\theta : \Omega \to \{0,1\}^k, 1 \geq \theta_1(x) \geq ... \geq \theta_k(x) \geq 0, \forall x \in \Omega\} \tag{2.30}$$

From the Equation 2.28, the following relation can be established:

$$\theta_i(x) - \theta_{i+1}(x) = \begin{cases} 1 \text{ if } u(x) = l \\ 0 \text{ otherwise} \end{cases} \tag{2.31}$$

with $\theta_0(x) = 1$ and $\theta_{k+1} = 0$ for simplification. Making use of the Equation 2.31, the data term of Equation 2.25 can be written in terms of θ as:

$$\sum_{i=0}^{k} \int_{\Omega_i} f_i(x)dx = \sum_{i=0}^{k} \int_{\Omega} (\theta_i(x) - \theta_{i+1}(x)) f_i(x)dx \tag{2.32}$$

Rewriting the regularizer term in terms of θ is not so straightforward. Simply summing the total variations of each function θ_i would imply that certain boundaries are counted more than once. An example is shown in Figure 2-9.b, the boundary between Ω_0 and Ω_2 would be counted twice. The dual formulation allows to suppress a multiple counting of boundaries when combined with an additional constraint on the dual variables [45]. The final formulation of Equation 2.25 in terms of θ becomes:

$$\min_{\theta \in B} \max_{\xi \in K} \left\{ \sum_{i=0}^{k} - \int_{\Omega} \theta_i \, div \, \xi_i \, dx + \int_{\Omega} (\theta_i(x) - \theta_{i+1}(x)) f_i(x)dx \right\} \tag{2.33}$$

with a set of $\xi = (\xi^0, ..., \xi^k)$ of dual vectors fields $\xi_i : \Omega \to R^2$, constrained to the set

$$K = \{\xi : \Omega \rightarrow R^{dxk}, |\sum_{i_1 \leq i \leq i_2} \xi_i(x)| \leq 1, \forall x \in \Omega, 1 \leq i_1 \leq i_2 \leq k\} \tag{2.34}$$

For a proof refer to [49]. The overall optimization problem in Equation 2.33 is non-convex because the set B defined in Equation 2.30 is not convex. But the same convexification as in the two-label case can be applied by relaxing the set of binary solutions to the set of functions which can take all values in $[0; 1]$. To this end the set B in the optimization problem 2.33 is replaced by the convex set:

$$R = \{\theta : \Omega \rightarrow [0, 1]^k, 1 \geq \theta_1(x) \geq ... \geq \theta_k(x) \geq 0, \forall x \in \Omega\} \tag{2.35}$$

For k = 1 this formulation turns out to be equivalent to the two-region problem considered for which we have optimality guarantee [50]. But for general problems of more than one region $k > 1$, the global optimality cannot be guaranteed but the optimilality bound can be found.

2.9 Conclusion

These techniques have been widely used in medical image segmentation and continuously improved to try to overcome their limitations. Model-free segmentation methods usually require user interaction and they are usually not robust to noisy or non-contrast data. In addition, they offer limited framework to incorporate prior knowledge. Deformable models are more flexible in this sense. However, the parametric deformable model also known as snakes has fixed topology or a complex scheme must be implemented to deal with topology changes. This issue can be alliviated using the level sets framework. Both snakes and level sets can get trapped into local minima because of many artifacts in medical images such as limited image contrast, the presence of noise as well as variations in anatomy and pathology. Graph cuts have recently become very popular due to its efficient global optimization, despite the difficulty to include high level information in the formulation of the graph cut

and the limitation to a set of energy functions. Active shape models seem robust to recognizing and locating known rigid objects in the presence of noise, clutter, and occlusion. But the creation of a training set is a tedious and time-consuming task and the accuracy of the segmentation relies in the variability of the training data set. The same occurs with atlas-based techniques whose main issue is that there is no anatomical constraint incorporated, making the atlas have little influence in the segmentation. Nowadays, convex optimization is getting much attention in research in the computer vision field due to the robust tools available to solve convex problems. But finding the equivalent convex problem to the original one is often not trivial and the solution of the convex problem may not be the optimum in the original one.

As reviewed, all methods have their pros and cons and the choice of one or another depends more on the application itself and the expertise of the person who chooses it. Petitjean et al. [3] wrote a very interesting review of these methods applied to short-axis cardiac MR images. They also included an assessment of segmentation accuracy based on MICCAI 2009 challenge studies. According to the results in the MICCAI challenge 2009, the authors draw some conclusions. The methods with better results were model-free techniques [51, 52]. However these techniques required user interaction and could not asses the ventricular surface in all phases. Other works based on ASM [53] or model-free-based methods using registration and minimum surfaces [54] offered a good compromise between performance and ambiguity. Other approaches were interesting too such as the one of Constantinides using snakes [55] but they were left ventricle specific and not applicable to the right ventricle. Whereas, there were other approaches with more generic methodologies such as the O'Brien's work with a couple ASM [53]. For a more detailed comparison of the methods, please refer to [3] and to [13] for additional information of segmentation methods including deformable models and graph-based image segmentation approaches.

Chapter 3

Shape Model Techniques

Shape modelling is an important aspect of computer graphics as well as computer vision research. The goal of shape modelling is to find a few features which describe as many shape details as possible. Shape models have been widely used successfully for tasks of object representation, shape reconstruction and recognition among others. In this Chapter, we will describe the main techniques for modelling data including data alignment and shape variations as well as how to incorporate shape model information in our work.

3.1 Shape and Landmarks

Shape can be defined as all geometrical information that remains when location, scale and rotational effects are filtered out from an object [56]. In other words, the objects' shape is invariant to Euclidean transformations such as translation, rotation and scaling. One way to describe a shape is by a finite number of points on the outline called landmarks. A landmark is a point of correspondence on each object that matches between and within populations and can be categorized into [57, 58]:

1. Anatomical landmarks: Points are assigned by an expert that corresponds between objects of study in a meaningful disciplinary context.

2. Mathematical landmarks: Landmark points are located on an object according

to some mathematical or geometrical property of the figure, i.e. high curvature or an extremum point.

The representation for an n-point shape consists of a $k \times p$ matrix of coordinates, where p is the number of landmark points and k is the dimensionality of the physical space. The order is arbitrary $x = [x_1, y_1, x_2, y_2, ..., x_p, y_p]$.

3.2 Procrustes for Shape Alignment

To compare two shapes, the location, scale and rotational transformations need to be filtered out. This is carried out by establishing a coordinate reference commonly known as pose to which all shapes are aligned [58]. A common method for this purpose is known as Procrustes analysis [57, 59, 60, 61]. The objective is to obtain a similar placement and size to a target shape, by minimizing a measure of shape difference called the Procrustes distance between the objects. The Procrustes distance to align two shapes x_1 and x_2 is computed as follows [58]:

1. The centroid of all objects are calculated by averaging the components x and y of the landmarks: $(\overline{x}, \overline{y}) = \left(\frac{1}{n}\sum_{j=1}^{n} x_j, \frac{1}{n}\sum_{j=1}^{n} y_j\right)$.

2. Center all the shapes on the origin so that their means become zero by subtracting the respective centroid from all landmarks.

3. Re-scale each shape to have equal size (usually unit size or $size = 1.0$). To do so, each object is divided by its centroid size S. The centroid size is defined as the square root of the summed squared distances of each landmark to the centroid $S(x) = \sqrt{\sum_{j=1}^{n}[(x_j - \overline{x})^2 + (y_j - \overline{y})^2]}$. Centroid size can be thought as the standard deviation of the landmarks around the mean.

4. Rotate a shape to align it to the other around the origin until the sum of squared distances between them is minimized:

   (a) Arrange the size and position aligned of the two shapes x_1 and x_2 as $n \times k$ matrices.

(b) Calculate the singular value decomposition UDV^T of $x_1^T x_2$ in order to maximize the correlation between the two sets of landmarks.

(c) The rotation matrix needed to optimally superimpose x_1 upon x_2 is then VU^T:

$$VU^T = \begin{pmatrix} cos(\theta) & -sin(\theta) \\ sin(\theta) & cos(\theta) \end{pmatrix}$$

(d) Minimize the sum of the squared point distances which is also known as squared Procrustes distance $P_d^2 = \sum_{j=1}^{n}[(x_{j1} - x_{j2})^2 + (y_{j1} - y_{j2})^2]$.

An example of Procrustes algorithm between two shapes is shown in Figure 3-1.

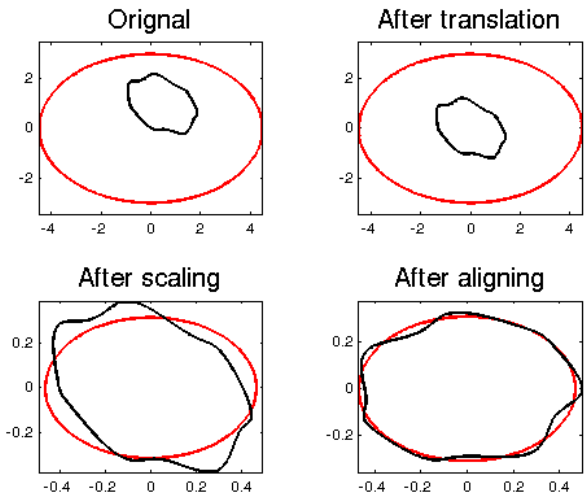

Figure 3-1: Procrustes example between two shapes showing intermediate results after translation, scaling and rotation. (Author: Alex Townsend)

In case we have more than two shapes to align, a simple iterative approach can be used to obtain the generalized procrustes analysis [30, 58, 62]:

1. Choose the first shape as an estimate of the mean shape.
2. Align all the remaining shapes to the mean shape.
3. Re-calculate the estimate of the mean from the aligned shapes using $\overline{x} = \frac{1}{N}\sum_{i=1}^{N} x_i$ where N denotes the number of shapes.
4. If the mean estimate has changed return to step 2.

3.3 Modelling Shape Variations

Principal Component Analysis (PCA) introduced by Pearson [63] in 1901 and Harold Hotelling in 1933 [64] has been widely used to describe the main directions of shape variations in a training set. In general, PCA looks for linear combinations of the original features which can be used to represent the data, losing in the process as little information as possible. Since this process reduces the dimensionality of the dataset, and hence makes the interpretation easier, it is an useful tool in shape analysis. The PCA process is achieved by transforming a data set consisting of a large number of interrelated variables into a new set of variables, the principal components, which are uncorrelated and ordered so that the first few retain most of the variation present in all of the original variables [65].

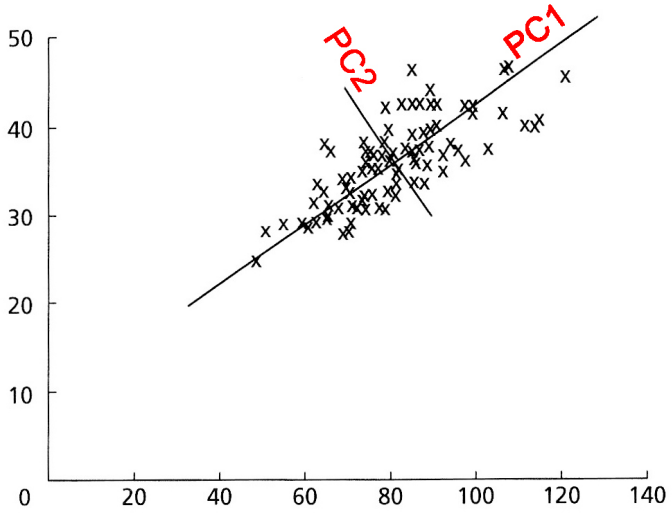

Figure 3-2: PCA example in 2D: The principal components of a data set are its major axes. (Author: Swan and Sandilands)

Conceptually the PCA performs a variance maximizing rotation of the original variable space and provides the new axes ordered according to their variance [58]. An example is shown in Figure 3-2, where the two principal axes of a two dimensional data set are plotted and scaled according to the amount of variation explained by each axis. Hence, the PCA can be used for dimensionality reduction by projecting a set of multivariate samples into a subspace constrained to explain a certain amount of

the variation in the original samples. In connection to the example in Figure 3-2, one could choose to visualize the samples by providing an orthogonal projection of the points upon the first (and largest) axis while the second principal axis is discarded. In addition to dimension reduction, PCA can be used to determine any underlying variables or to identify intra-class clustering or outliers [58].

Principal components are the linear combination of the centered original variables. Given a data matrix with p variables and n samples, the data are first centered on the means of each variable. This will ensure that the cloud of data is centered on the origin of the principal components. The first principal component (y_1) is given by the linear combination of the variables $x_1, x_2, ..., x_p$ [66]:

$$y_1 = m_{11}x_1 + m_{12}x_2 + ... + m_{1p}x_p \tag{3.1}$$

or in matrix notation:

$$y_1 = m_1^T X \tag{3.2}$$

The first principal component is calculated such that it accounts for the highest possible variance in the data set. Obviously, the variance of y_1 could be made as large as possible by choosing large values for the weights m. To prevent this issue, weights are calculated with the constraint that their sum of squares is 1.

$$m_{11}^2 + m_{12}^2 + ... + m_{1p}^2 = 1 \tag{3.3}$$

The second principal component is computed in the same way, with the condition that it is uncorrelated with (i.e., orthogonal to) the first principal component and that it accounts for the second largest amount of variance.

$$y_2 = m_{21}x_1 + m_{22}x_2 + ... + m_{2p}x_p \tag{3.4}$$

This continues until a total of p principal components have been calculated, equal to the original number of variables [66].

Collectively, all these transformations of the original variables to the principal components are defined as:

$$Y = MX \tag{3.5}$$

where the matrix M contains the eigenvectors of the covariance matrix of the original data and the elements of an eigenvector are the weights m_{ij}. Eigenvectors provide the weights to compute the uncorrelated principal components.

To seek the linear transformation of the data, first we consider the mean shape $\overline{x} = \frac{1}{N}\sum_{i=1}^{N} x_i$ and the shape covariance matrix [58]:

$$\Sigma_x = \frac{1}{N}\sum_{i=1}^{N}(x_i - \overline{x})(x_i - \overline{x})^T \tag{3.6}$$

The mean of the y-variables can then be expressed as:

$$\overline{y} = \frac{1}{N}\sum_{i=1}^{N} y_i = \frac{1}{N}\sum_{i=1}^{N} Mx_i = M\overline{x} \tag{3.7}$$

And consequently the covariance of the y's:

$$\begin{aligned}
\Sigma_y &= \tfrac{1}{N}\textstyle\sum_{i=1}^{N}(y_i - \overline{y})(y_i - \overline{y})^T \\
&= \tfrac{1}{N}\textstyle\sum_{i=1}^{N}(Mx_i - M\overline{x})(Mx_i - M\overline{x})^T \\
&= \tfrac{1}{N}\textstyle\sum_{i=1}^{N} M(x_i - \overline{x})(M(x_i - \overline{x}))^T \\
&= \tfrac{1}{N}\textstyle\sum_{i=1}^{N} M(x_i - \overline{x})(x_i - \overline{x})^T M^T \\
&= M\left(\tfrac{1}{N}\textstyle\sum_{i=1}^{N}(x_i - \overline{x})(x_i - \overline{x})^T\right) M^T \\
&= M\Sigma_x M^T
\end{aligned}$$

Then, we limit to orthogonal transformation by left-multiplying by M^T:

$$M^T\Sigma_y = \Sigma_x M^T \tag{3.8}$$

Substitution of M^T by ϕ yields:

$$\Sigma_x\phi = \phi\Sigma_y \tag{3.9}$$

The covariance matrix of the principal components, is known as the eigenvalues with the elements in the diagonal of matrix. Eigenvalues are the variance explained by each principal component, and are constrained to decrease monotonically from the first principal component to the last [66]. From Equation 3.9 it is seen that if ϕ is chosen as the (column) eigenvectors of the symmetric matrix Σ_x, then the covariance of the transformed shapes Σ_y becomes a diagonal matrix of eigenvalues [58]. In the case of correlated points the smallest eigenvalues will be zero or close to zero and the corresponding eigenvectors can be discarded from ϕ thus reducing the length of y.

In order to back transform from the new set of variables, y, one can invert Equation 3.5, considering that M is orthogonal:

$$x = M^{-1}y = M^{T}y = \phi y \tag{3.10}$$

Generally, PCA is applied on variables with zero mean (notice that the ϕ is unchanged) [58]:

$$y = M(x - \overline{x}) \ , \ x = \overline{x} + \phi x$$

Given the mathematical explanation of PCA, we define the PCA procedure as follows:

1. Subtract mean from each shape. This produces a data set whose mean is zero.

2. Calculate covariance matrix to estimate variance and covariance among the original variables.

3. Calculate eigenvalues and eigenvectors of covariance matrix and find the major axes of the data and the variation among them.

4. Rotate the original data onto the major axes and give the coordinates for their new position.

Graphically, the PCA process is shown in Figure. 3-3.

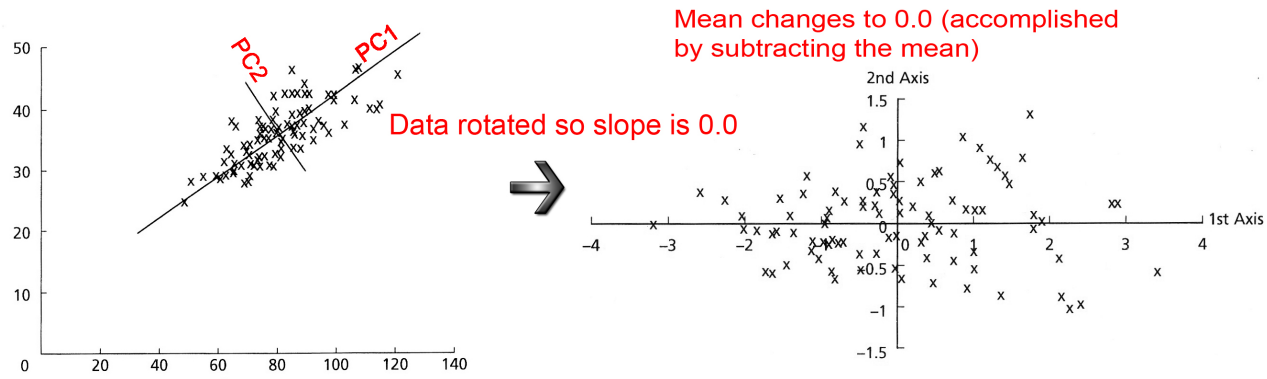

Figure 3-3: PCA procedure: Rotates data to its major axes preserving original distances between data points and removing correlations between variables.

Independent Component Analysis (ICA) [67] is an alternative method for the construction of the modes of shape variation which does not assume a normal distribution of the input data in contrast to PCA which supposes that the training data is from a Gaussian distribution, which often is not the case. One of the main differences between these two methods is that in PCA the objective is to find the modes of shape variation that explain maximal amount of the variance in the training set, whereas in ICA, the independency of the modes of shape variation is maximized. Furthermore, in PCA the objective is to find global shape variations, whereas in ICA the objective is to show localized shape variations [68]. In the context of statistical shape models, ICA was recently introduced by Üzumcü et al. who used ICA to construct a statistical shape model from a 2-D cardiac data set [69], and used it in 2-D cardiac segmentation [70]. Several different methods for calculating ICA exist, such as the FastICA [71], the InfoMax [72] and the JADE [73] algorithm. These methods differ in the optimized contrast function to achieve decorrelation [74].

In classical PCA, one is able to define a natural ordering of the eigenvectors according to the associated eigenvalues (variances). Therefore, it is possible to obtain a compact description of the shape set by discarding the eigenvectors describing the least variance [75]. In Independent Component Analysis however, the directions are known to be descriptive of independent factors but the method itself does not provide any order or ranking of components. This makes it difficult to achieve dimensionality reduction unless, as customarily, one first performs PCA [74, 75, 76].

When the shape space is nonlinear, as in the case when large pose variations are allowed, linear transformation methods such as ICA or PCA can still address the shape model problem to some extend by approximations using a combination of linear components [30, 77, 78]. However, the use of linear components increases the dimensionality of the model and also allows for non-valid shapes [79, 80]. Although nonlinear shape variation can be captured by a set of structured linear models using hierarchical principal components [81], this requires a very large database for learning the distribution of the linear subspaces [80]. Kernel Principal Component Analysis (KPCA) is a nonlinear PCA method. In general, PCA can only be efficiently used on a set of observed data that vary linearly. When the variations are nonlinear, they can always be mapped into a higher dimensional space which is again linear. If this higher dimensional linear space is referred to as the feature space (F), Kernel PCA utilizes a kernel function which intrinsically constructs a nonlinear mapping from the input space to F [80]. As a result, KPCA performs a nonlinear PCA in the input space.

Like PCA, ICA is based on a linear model, so it is inadequate for ICA to describe complex nonlinear variations due to illumination changes, viewpoint changes and noise [82]. One approach to solve this problem is again to use kernel-based methods as they are effective for such non-linearity. Kernel methods allow for the development of a non-linear extension of some linear algorithms, such as PCA and ICA. Recently, Kernel ICA (KICA) [83] was proposed as a nonlinear extension of ICA, which combines a nonlinear kernel with ICA by mapping the input image data into an implicit feature space F, and then ICA is performed in F to produce nonlinear independent components of input data.

3.4 Statistical Shape Models

Statistical shape models such as Active Shape Models (ASM) or Active Appearance Models (AAM) have shown great potential in image recognition and segmentation tasks. Such models generally use Principal Component Analysis to describe the main

directions of shape variation in a training set of example shapes. These models describe statistical variations in a set of training images, in which corresponding landmark points are annotated. First, the shapes, which are spanned by the landmarks, are aligned, e.g., using Procrustes analysis. Then, the mean shape of this set of aligned shapes is computed, and modes of shape variation are calculated using PCA. Each shape sample can then be expressed by means of a set of shape coefficients v as follows [74]:

$$x \sim \mu + Uv$$

where x is a shape sample, μ the mean shape, U contains the eigenvectors describing the modes of shape variation in the training set and v is the vector containing the coefficients weighting those eigenvectors. Refer to Chapter 2.5 for more details.

3.5 Shape Model for Prior Computation

The structure of shape spaces and statistical shape analysis have been examined in different applications range from the computation of priors for segmentation and shape classification to the construction of standardized anatomical atlases.

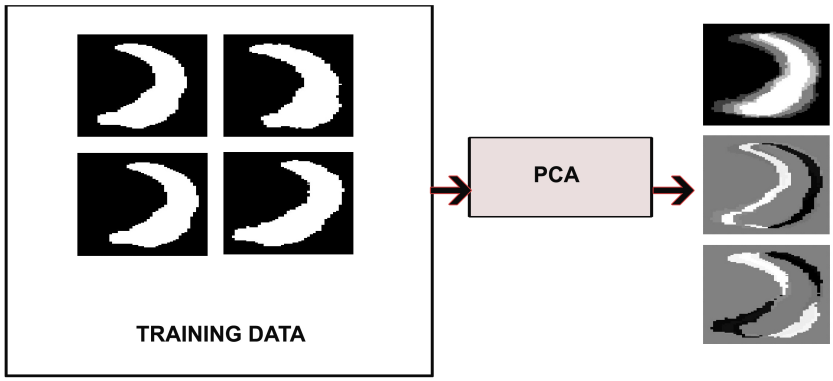

Figure 3-4: Example of the proposed PCA which gives as a first component the average shape and the shape variation for the rest of components.

The focus of our research has been the application of shape analysis for computation of priors. In particular, we use principal component analysis in the technique of normalized cuts with shape prior. We are interested in obtaining as the first compo-

nent the average shape and for the rest of components the shape variation. For this purpose, we change the PCA method as follows:

1. A matrix of priors P is given where the priors are kept in columns.
2. Calculate the eigenvectors of $P^\top P$.
3. Multiply the matrix P with the eigenvectors.
4. Normalize the result.

An example of using the proposed PCA shape model is shown in Fig. 3-4. Given a training data with translations and rotations, the projection of the training data over the eigenvectors give as a first component an average shape and the others show the shape variation of that average shape.

Chapter 4

Normalized Cuts with Shape Priors

4.1 Introduction

Normalized cuts [84] is an efficient graph theoretic segmentation method robust to noise and outliers, and is thus a good candidate for medical imaging segmentation. Previously, it has been used for segmentation of the spinal vertebrae [85] and clustering of white matter fiber tracts [86] among others. Although normalized cuts has not become as popular in the medical segmentation field as other methods such as level sets [21] or graph cuts [32] due to the difficulty and limitation to add prior knowledge, it has been widely used for natural images giving promising results.

The prior can provide valuable information combined with low level cues (e.g., similarity of pixel brightness, color, texture and motion) to guide the segmentation to extract an object of interest from an image. There are some techniques to incorporate prior knowledge into normalized cuts but they are still limited. In [87], Yu et al. model the prior as a linear constraint on a partial grouping solution indicating which pixels should belong to one partition. They also impose a uniformity condition on the constraints by propagating grouping information from labeled nodes to their neighbors to obtain smooth solutions. In their later work, the authors reformulate the normalized cut method to seek among the segmentations determined by partial

constraints the one that optimizes the goodness of grouping and enforces grouping smoothness for effective propagation [88]. In addition, the authors argue that the main differences with other works of clustering incorporating constraints are that instead of instantiating the labels or the constraints on labeled data points, they use the labels to regulate the form of the segmentation, and that unlike most of the works, they can guarantee local near-global optima.

Eriksson et al. propose a reformulation of the relaxation of normalized cuts through a Lagrangian dual formulation to handle all types of linear equality constraints for any number of partitions [89]. However, Maji et al. show that this method is not robust when the constraints are noisy and propose a new formulation which in addition requires the solution to have sufficient overlap with the "prior guess" [90]. This formulation allows seeking solutions sufficiently correlated with the prior with a small amount of additional time. Tolliver et al. argue that spectral relaxation approximations suffer from spurious structures introduced by the constraints on the eigenvectors that may produce poor solutions [91]. They propose to introduce shape constraints by iteratively aligning the eigenvector space with the current estimation of the shape and then updating the shape estimate by fitting regions that are likely to contain the cut. Cai's work [92] is inspired by Tolliver's method [91] and modifies all the relationships between nodes using shape constraints to make more flexible the adjustment of the algorithm at the level of pairwise pixels.

We present a novel method to integrate shape prior knowledge into normalized cuts. The proposed method seeks the normalized cut while maximizing the association of the prior within a group and the disassociation with the other. Our main contribution is that the prior is included into the cost function without the inclusion of hard constraints avoiding the issues described above [91]. Furthermore, depending on the application, the method does not require the inclusion of spatial relationships, because they are already in the prior term and it can be extended easily to deal with multiple priors applying Principal Component Analysis (PCA). The Spectral Relaxation of the problem provides an efficient solution, although the resulting eigenproblem is not sparse. The results of our method are very promising even when the

image is noisy with limited contrast or the prior is inaccurate whereas most of the previous methods require a reliable prior. We also adapt the proposed method on natural images and compare it with the latest methods in normalized cuts with prior.

4.2 Theory

Graph-based segmentation algorithms are based on the representation of an image as an undirected weighted graph where the pixels of the image are the nodes and the edges have weights that represent the similarity between nodes. A measure of similarity can be established considering pairwise pixel features like intensity, color, texture and distance. Each edge is represented in the affinity matrix W that represents the connections between nodes. The graph can be partitioned into two disjoint sets by using the normalized cuts criterion, where the similarity among the nodes in the same set is high and across different sets is low.

Let Ω be the set of all nodes and $w_{ij} = (\mathbf{W})_{ij}$ the affinity matrix. The cut is defined as the degree of dissimilarity between two partitions computed as the total weight of the edges that separates the graph into two disjoint sets:

$$\text{cut}(A, B) = \sum_{i \in A, j \in B} w_{ij}$$

As this minimum cut criterion tends to cut small sets of isolated nodes in the graph, Shi and Malik [84] proposed the normalized cut criterion obtained by computing the cut cost as a fraction of the total edge connections to all the nodes in the graph and the partition selected is the one that minimizes this cost:

$$\text{Ncut}(A, B) = \frac{\text{cut}(A, B)}{\text{bal}(A, B)}$$

where the balance of the two sets is defined by $\text{bal}(A, B) = \left(\frac{1}{V(A)} + \frac{1}{V(B)}\right)^{-1}$ and V is the total edge connections to all the nodes in the graph: $V(A) = \sum_{i \in A, j \in \Omega} w_{ij}$. Note that $V(A) = \text{cut}(A, \Omega)$ and the normalized cut solutions will favor minimum cuts

with higher balance values. To minimize the normalized cut, the authors developed an algorithm, which is based on the solution of a generalized eigenvalue problem. Let $(\mathbf{x})_i = x_i$ be an indicator vector where $x_i = 1$ for $i \in A$ and $x_i = -1$ for $i \in B$. Let $d_i = \sum_j w_{ij} = (\mathbf{D})_{ii}$, be the diagonal matrix that defines the connection of every node to all other nodes. By setting: $\mathbf{y} = (\mathbf{1} + \mathbf{x}) - b(\mathbf{1} - \mathbf{x})$, Shi and Malik deduced the following minimization criterion:

$$\min_{\mathbf{y}} \quad \frac{\mathbf{y}^\top(\mathbf{D} - \mathbf{W})\mathbf{y}}{\mathbf{y}^\top\mathbf{D}\mathbf{y}}$$

with conditions $y_i \in \{1, -b\}$ and $\mathbf{y}^\top\mathbf{D}\mathbf{1} = 0$ where b is a constant less than 1. The problem of minimizing the normalized cut is NP hard. However, the authors have demonstrated that the minimization of this criterion can be approximated by relaxing y to take all real values and solving the eigenvector problem of $\mathbf{D}^{-1/2}(\mathbf{D} - \mathbf{W})\mathbf{D}^{-1/2}$ where the eigenvector with the second smallest eigenvalue approximates the optimal normalized cut solution.

4.2.1 Introducing the Prior

We want to incorporate the prior information, a set of points belonging to the same group, into the normalized cut formulation by minimizing the normalized cut criterion and at the same time, maximizing the association of the prior to one partition and disassociation to the other.

Let C be a set of points that make up the prior and that should be contained either in the partition A or B. We know a-priori that $\Omega = A \cup (\Omega \setminus A)$ where $B = (\Omega \setminus A)$. Therefore, we would like the solution such that either the intersection of A and C or the intersection of B and C is large. To be more precise we want the *relative* overlap respectively, to be large. The volume of the absolute intersection $V(A \cap C)$ is obviously not a good choice, as Ω would already maximize the objective. Therefore, we use the relative overlap which is defined as follows:

$$P_C(A) = \frac{V(A \cap C)}{V(A)} \quad \text{or} \quad P_C(B) = \frac{V(B \cap C)}{V(B)}$$

The above defined relative overlap $P_C(A)$ is maximized for $P_C(A = C) = 1$ (the same idea with B), which is our intention. Now, we have to formulate that we are interested in exclusively having $P_C(A)$ or $P_C(B)$ large, and not mutually. One way is to require that the squared difference $(P_C(A) - P_C(B))^2$ is large, which requires one of them to be large and the other to be small. We combine this with the original Ncut objective as follows:

$$\text{Pcut}_{C,\gamma}(A, B) = \frac{\text{Ncut}(A, B)}{1 + \gamma^2 \text{ bal}(A, B) \cdot (P_C(A) - P_C(B))^2}$$

where γ is the parameter which controls the influence of the prior. The additional multiplicative dependence on $\text{bal}(A, B)$ controls that, if the solution is far off from the normalized cut, the influence of the prior is reduced.

This formulation also allows to be extended to fuzzy sets in a straightforward way as well as express the prior as a linear combination of overlaps. Suppose there are several priors, i.e. several C_k with $k = 1, \ldots, N$. Then, we can generalize the above objective to:

$$\text{Pcut}_{C,\gamma}(A, B) = \frac{\text{Ncut}(A, B)}{1 + \text{bal}(A, B) \cdot \sum_{k=1}^{N} \gamma_k^2 (P_{C_k}(A) - P_{C_k}(B))^2}$$

where we have a sum of squared distances of the relative overlap with groups A and B for every prior C_k. Furthermore, let c_i with $i \in \Omega$ be a set of positive weights expressing the 'amount' of membership of pixel i to C and $d_i = \sum_{j \in \Omega} w_{ij}$. Then we can define $P_C^{fuzzy}(A) = \frac{\sum_{i \in \Omega} c_i \ d_i}{V(A)}$ as the 'fuzzy' relative overlap. Also note, that there is no necessity for the weights c_i of being positive. In fact, it is possible to use the principal components of a PCA shape model as priors, i.e. $P_{C_k}(A) = \frac{\sum_{i \in \Omega} c_i^k \ d_i}{V(A)}$, where $(\mathbf{c}_k)_i = c_i^k$ are the k-th principal components of the shape model.

We want to compute PCA and get the average shape as the first principal component and the shape variations for the rest of components. For that, we need to change slightly the traditional PCA described in Section 3 following these steps:

1. A matrix of priors P is given where the priors are kept in columns.

2. Calculate the eigenvectors of $P^\top P$.

3. Multiply the matrix P with the eigenvectors.

4. Normalize the result.

An example of using the principal components of a PCA shape model as a shape prior is shown in Fig. 4-1. Given a training data with translations and rotations, the proposed PCA gives as a first component an average shape and the others show the shape variation around that average shape. The principal components can be used as a prior c_k.

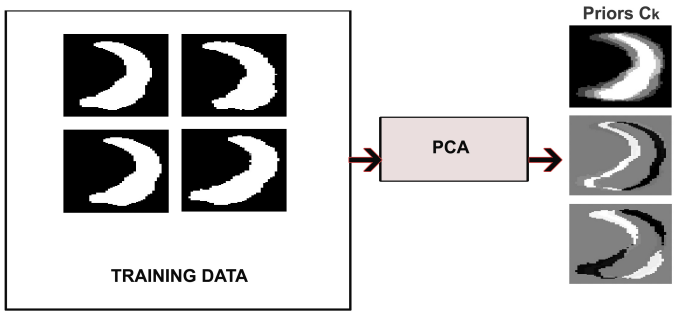

Figure 4-1: Example of using the principal components as a shape prior.

4.2.2 Spectral Relaxation

Once we have introduced the prior to the normalized cut criterion, the solution is approximated by spectral relaxation. Let $(\mathbf{x})_i = x_i$ be an indicator vector for the set membership, i.e. $x_i = 1$ for $i \in A$ and $x_i = -1$ for $i \in B$. For short we write $\mathbf{x}_A = (1 + \mathbf{x})/2$ and $\mathbf{x}_B = (1 - \mathbf{x})/2$. Let $d_i = \sum_j w_{ij} = (\mathbf{D})_{ii}$ be the diagonal matrix with the row sum on the diagonal. Suppose a set of priors $(\mathbf{c}_k)_i = c_i^k$ is given. We want to minimize:

$$\min_{A \cap B = \emptyset, A \cup B = \Omega} \mathrm{Pcut}_{C,\gamma}(A, B)$$

By setting $\mathbf{y} = \frac{\mathbf{x}_A}{V(A)} - \frac{\mathbf{x}_B}{V(B)}$ we can show that the above problem is equivalent to:

$$\min_{\mathbf{1}^\top \mathbf{y}=0,\ y_i \in I} \quad \frac{\mathbf{y}^\top (\mathbf{D}-\mathbf{W})\mathbf{y}}{\mathbf{y}^\top \mathbf{D}\mathbf{y} + \sum_k \gamma_k^2 (\mathbf{y}^\top \mathbf{D}\mathbf{c}_k)^2}$$

where $(\mathbf{y})_i = y_i$ are allowed to take values in $I = \{-V(B)^{-1}, V(A)^{-1}\}$. Relaxing this constraint to $y_i \in \mathbb{R}$ we arrive, similarly to the ordinary Ncut, at the generalized Eigenproblem:

$$(\mathbf{D}-\mathbf{W})\mathbf{y} = \lambda(\mathbf{D} + \sum_{k=1}^{N} \gamma_k^2 \mathbf{D}\mathbf{c}_k\mathbf{c}_k^\top \mathbf{D})\mathbf{y}$$

To get an ordinary eigenvalue problem (which is computationally preferred) one usually sets $\mathbf{y}' = \mathbf{D}^{-1/2}\mathbf{y}$ and multiplies the above equation by $\mathbf{D}^{-1/2}$:

$$(\mathbf{I} - \mathbf{D}^{-1/2}\mathbf{W}\mathbf{D}^{-1/2})\mathbf{y}' = \lambda(\mathbf{I} + \sum_{k=1}^{N} \gamma_k^2 \mathbf{D}^{1/2}\mathbf{c}_k\mathbf{c}_k^\top \mathbf{D}^{1/2})\mathbf{y}'$$

which is, in our case, still a generalized eigenproblem. Using the substitution $\mathbf{p}_k = \gamma_k \mathbf{D}^{1/2}\mathbf{c}_k$ and $\mathbf{Q} = \mathbf{I} + \sum_k \mathbf{p}_k\mathbf{p}_k^\top$ the problem becomes:

$$(\mathbf{I} - \mathbf{D}^{-1/2}\mathbf{W}\mathbf{D}^{-1/2})\mathbf{y}' = \lambda\mathbf{Q}\mathbf{y}'$$

We can then use the same trick from above, that is, setting $\mathbf{y}'' = \mathbf{Q}^{-1/2}\mathbf{y}' = \mathbf{Q}^{-1/2}\mathbf{D}^{-1/2}\mathbf{y}$ which leads to the final eigenequation:

$$\mathbf{Q}^{-1/2}(\mathbf{I} - \mathbf{D}^{-1/2}\mathbf{W}\mathbf{D}^{-1/2})\mathbf{Q}^{-1/2}\mathbf{y}'' = \lambda\mathbf{y}''$$

The questions remains how to compute $\mathbf{Q}^{-1/2}$. Therefore, let $\mathbf{P}$ be the matrix where the prior vectors are stacked together as columns $\mathbf{P} = [\mathbf{p}_1, ..., \mathbf{p}_N]$. Then, let $\mathbf{P}_0$ be the matrix $\mathbf{P}_0 = \mathbf{P}(\mathbf{P}^\top\mathbf{P})^{-1/2}$, which is the orthogonal projection onto the space spanned by the prior vectors $\mathbf{p}_k$. Then, $\mathbf{Q}^{-1/2}$ is given by:

$$\mathbf{Q}^{-1/2} = \mathbf{I} + \mathbf{P}_0\left((\mathbf{I}_N + \mathbf{P}^\top\mathbf{P})^{-1/2} - \mathbf{I}_N\right)\mathbf{P}_0^\top$$

which is still efficient to apply, because $\mathbf{P}_0$ is a rank-N matrix, with the number of priors N in a moderate range.

4.3 Implementation

Efficient eigenvalue solvers (like Lanczos [84]) solely require the computation of the system matrix $\mathbf{A} = \mathbf{Q}^{-1/2}(\mathbf{I} - \mathbf{D}^{-1/2}\mathbf{W}\mathbf{D}^{-1/2})\mathbf{Q}^{-1/2}$. In our case, the computation of $\mathbf{A}$ is split into three parts: applying $\mathbf{Q}^{-1/2}$, then the ordinary graph-laplacian and once again $\mathbf{Q}^{-1/2}$. As already stated above, the application of $\mathbf{Q}^{-1/2}$ can be implemented efficiently as it consists of multiplications with the low-rank matrix $\mathbf{P}_0$.

4.4 Experimental Evaluation

The proposed method is tested on three different kinds of datasets, two biomedical segmentation tasks and one set of natural images from the person category of the PASCAL VOC 2011 [93]. Our method is compared with the latest techniques in constrained normalized cuts for prior incorporation such as partial grouping with normalized cuts by Yu and Shi [88] and biased normalized cuts by Maji, et al. [90]. The biased normalized cuts and the partial grouping approaches use the feature similarity term as a similarity measure and the spatial proximity term weighted probabilistically with the high dimensional Gaussian distribution as follows:

$$\mathbf{w}_{ij} = e^{\frac{-||\mathbf{F}(i)-\mathbf{F}(j)||_2^2}{\sigma_I^2}} * \begin{cases} e^{\frac{-||\mathbf{X}(i)-\mathbf{X}(j)||_2^2}{\sigma_X^2}}, & \text{if } ||\mathbf{X}(i) - \mathbf{X}(j)||_2 \text{ is } <\text{R} \\ 0, & \text{otherwise} \end{cases}$$

where w_{ij} reflects the similarity between two pixels, $X(i)$ is the spatial location of node i, R is the neighbourhood radius considered, σ is the standard deviation and $F(i)$ is a feature vector. Our approach only uses the feature similarity term, and the spatial proximity term may be omitted as this information is contained in the prior information. Additionally, we also compare with the implementation of biased normalized cuts with intervening contour cue also used in the authors' work

to compute the weight matrix. The code for computing biased normalized cuts on images is available at the authors website [94]. All parameters are optimized manually for all approaches.

4.4.1 Segmentation of Biomedical Data

We first test our method with T1-weighted MR-images of the left ventricle in the human brain. The ventricular system is a set of structures containing cerebrospinal fluid in the brain and we are interested in the lateral ventricle to test our algorithm. The region of interest is manually chosen such that the ventricle is approximately centered in the image with size 87x45 pixels and resolution 1x1 mm. The ground truth is created by using a data set of 10 manually segmented frames and replicated ten times by applying small affine distortions. From the ground truth labeling, a PCA shape model is built and used as a prior as described above. For testing purposes, we use 100 test images created in the same way as the ground truth.

Our approach, the intensity-based biased normalized cuts and the partial grouping approaches use the brightness feature as a feature vector based on intensity with F(i)=I(i).

Visual results are shown in Fig. 4-2. In the first and second rows, we observe similar results. In the third and fourth rows, we show a case where the shape prior is far away from the true segmentation. While our method is still able to cope with the 'bad' prior, all other methods have severe problems. In spite of that, we can also observe that when the prior is not accurate Maji's approach improves the performance of the partial grouping algorithm giving a better segmentation.

We also tested our algorithm to segment the myocardium. The detection of the myocardium is very challenging because of signal loss, the presence of papillary muscles and that the borders are in contact with other organs that have similar intensities. In our approach, a segmented cardiac data set of 26 frames is used to build the shape model. The other approaches use a circular Hough transform [95] to detect roughly two circular contours, which are used as a prior. To reduce the Hough transform complexity and increase its efficency, we scale the images to 32x32 pixels. All algorithms

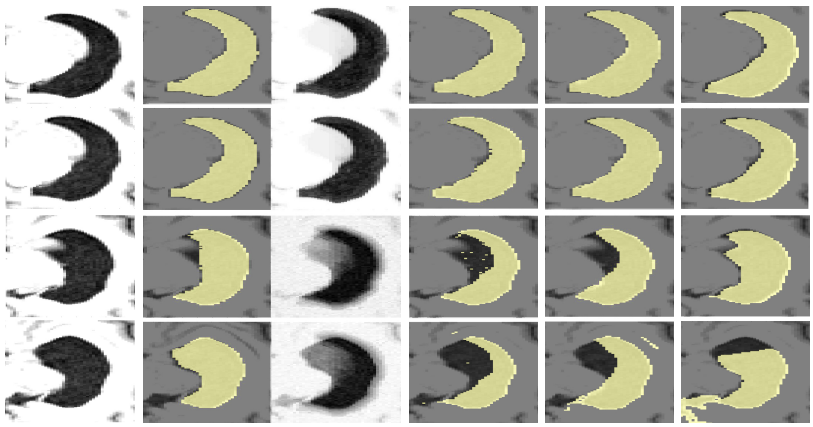

Figure 4-2: Segmentation of the left ventricle. (a) Original image. (b) Our method with its corresponding ncut-vector. (c) Partial grouping. (d) Intensity based-Bias Ncut. (e) Intervening contour based-Bias Ncut.

have been tested for twenty data sets of different patients between 26 frames and 57 frames in each sequence showing the contraction and expansion of the heart. The spatial resolution of every frame is 1.3 mm x 1.3 mm and the temporal resolution is 64 ms [96]. As we can see in Fig. 4-3 the results are more accurate with our method with less outliers giving a more compact segmentation. With respect to the other techniques we are comparing with, we found partial grouping more sensitive to the prior. In spite of that, in cases where the prior was sufficiently accurate the results could outperform the performance of biased normalized cuts as shown in Fig. 4-3.c.

	Left Ventricle			
	New	PG	BNC_i	BNC_{ic}
Distance (voxel)	1.01	2.33	2.71	2.04
Overlap	0.88	0.66	0.68	0.77
Sensitivity	0.93	0.81	0.92	0.93
Specificity	0.98	0.92	0.86	0.92
Similarity	0.93	0.78	0.80	0.87

Table 4.1: Average performance measures for the left ventricle, for the proposed approach (New), (PG) Partial Grouping, (BNC_i) Intensity based-Biased Ncut, (BNC_{ic}) Intervening contour based-Bias Ncut.

To quantify the segmentation quality assessment for every method we compute

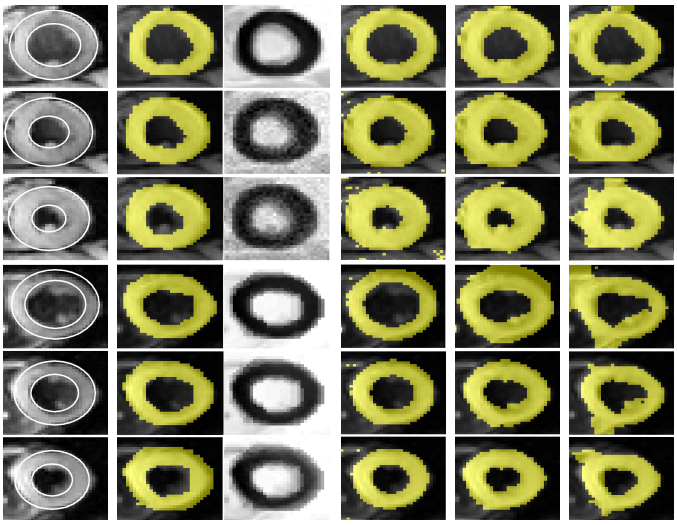

(a) (b) (c) (d) (e)

Figure 4-3: Segmentation of the heart. (a) Original image with single prior. (b) Our method and its normalized cut. (c) Partial grouping by Yu's method. (d) Intensity based-Bias Ncut. (e) Intervening contour based-Bias Ncut.

	Myocardium			
	New	PG	BNC_i	BNC_{ic}
Distance (voxel)	0.70	1.59	1.62	1.55
Overlap	0.78	0.65	0.62	0.60
Sensitivity	0.88	0.88	0.94	0.85
Specificity	0.92	0.76	0.69	0.74
Similarity	0.87	0.78	0.75	0.74

Table 4.2: Average performance measures for cardiac sequences, for the proposed approach (New), (PG) Partial Grouping, (BNC_i) Intensity based-Biased Ncut, (BNC_{ic}) Intervening contour based-Bias Ncut.

different performance measures: point to mesh distance [97] and overlap, sensitivity, specificity and similarity [1] [98]. The parameter setting for all techniques is $\sigma_I = 0.4$ and $\sigma_I = 0.6$ for the left ventricle and the myocardium respectively. The methods using spatial location term are set to $\sigma_X = 5.0$ and R is equal to the maximum number of neighbours. The number of eigenvectors of the PCA shape model used as a prior for our approach is six with $\gamma = 10$ for the left ventricle and $\gamma = 100$ for the

[1]The performance measures are defined as: $Overlap = \frac{TP}{TP+FN+FP}$, $Sensitivity = \frac{TP}{TP+FN}$, $Specificity = \frac{TN}{TN+FP}$ and $Similarity = \frac{2TP}{2TP+FN+FP}$ where TP and FP stand for true positive and false positive and TN and FN for true negative and false negative.

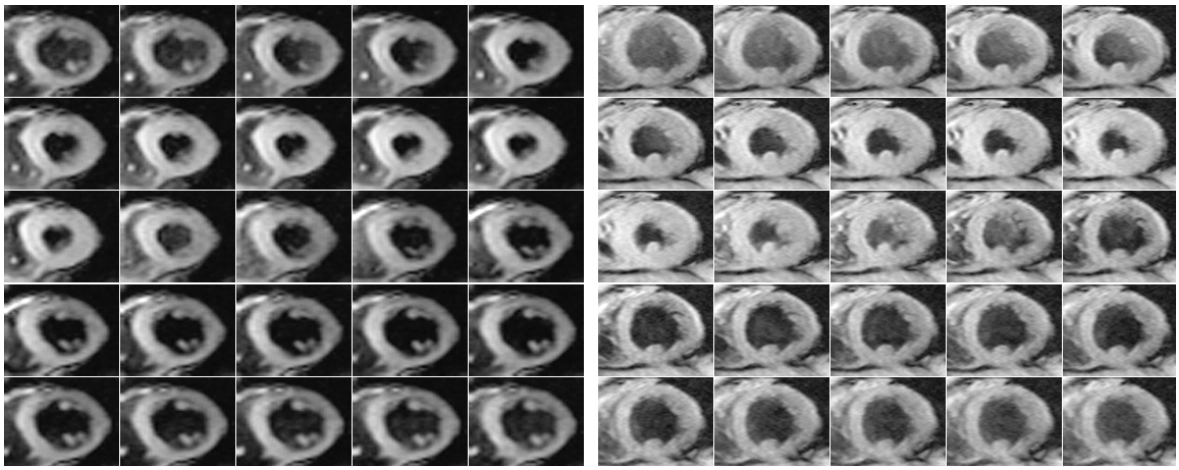

(a)

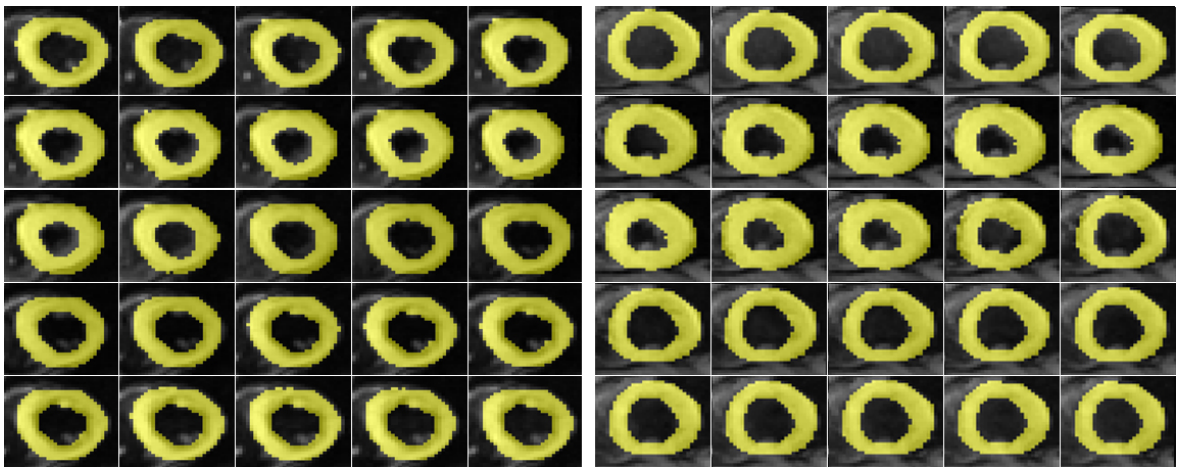

(b)

Figure 4-4: Segmentation of the myocardium with our method. (a) Original images. (b) Segmentation in white.

heart where γ is the weight for the prior.

Table 4.1 and Table 4.2 summarize the average performance for the left ventricle and the myocardium respectively where we can observe an improvement in all metrics tested for the ventricle and also for the myocardium except for some cases where either sensitivity (fraction of pixels belonging to the myocardium correctly detected) or specificity (fraction of pixels not belonging to the myocardium correctly detected) is higher but as the rest of the metrics are lower, they do not outperform the results of our method. The main reason for these promising results is that our algorithm includes shape variations into the formulation making it more robust to noise. In

addition, the proposed method does not only rely on a set of grouping points that may be noisy, something common in medical segmentation. We also found that partial grouping is more sensitive to the prior; although when the prior is adequate, it can slightly improve the biased normalized cut results in some cases. Moreover, biased normalized cuts based on intervening contour seems more accurate when the segmentation follows the edges like the left ventricle case whereas the intensity-based approach can improve the performance when the edges information cannot guide the segmentation propertly as shown in Fig. 4-3.e.

Another example for the myocardium segmentation using our method is shown in Fig. 4-4 for two different patients giving satisfactory results.

4.4.2 Segmentation of People

To demonstrate the performance of our idea on natural images we employed a category of the PASCAL VOC 2011 [93] where a ground truth segmentation is available and an automated method exists to get a prior that can be used during segmentation. We found the person category of the PASCAL VOC 2011 dataset as an ideal playground and used so called poselets [99] for detection and generation of the prior. Poselets capture parts of a pose and the key idea is to find which poselets are tightly clustered in both appearance of image patches and configuration space of keypoints. The implementation of the poselets and annotations for training are kindly provided by the authors [100]. One output of the poselet approach is a probability map for the presence of person in the scene, we will directly use this map as the prior in our approach. The region of interest is automatically defined around the output of the poselet object detector. We use 186 images of people where a ground truth segmentation is available. As the images are coloured we use HSV values for computing the affinity matrix. Specifically, we use the feature vector as follows [84]: $F(i) = [v, v \cdot s \cdot sin(h), v \cdot s \cdot cos(h)]$ and the usual Gaussian function as affinity function with $\sigma_I = 0.6$ for all methods and $\sigma_X = 5.0$ and R equal to the maximum number of neighbours for the ones using the spatial location term.

In Fig. 4-5, we can see some selected results of people segmentation. Our approach

Figure 4-5: Segmentation of colour images using the poselet object detector output as a prior for the proposed approach (New) with its corresponding normalized cut (Ncut), (BNC_{ic}) Intervening contour based-Bias Ncut and (PG) Partial Grouping.

gives a closer segmentation and a more precise foreground / background partition although the prior is not accurate. Moreover, we can observe that although Maji's technique may result in sharper segmentations following more the edges and the borders in some cases as shown in the last two rows of Fig. 4-5, this technique may not give you a precise bi-partition background / foreground. The same problem

occurs with the partial grouping which in addition suffers from high prior sensitivity causing a degradation of the segmentation due to the inaccuracy of the prior. This results in high sensitivities, as the prior usually includes the person to segment, but also low specificities, as the prior includes several points not belonging to the person. Moreover, this problem is also discussed in [88] where the authors argue that their formulation can neither spot nor correct mistakes in priors and that the extent of this detrimental effect depends on the connections of the constrained nodes, since partial grouping information is propagated to neighboring nodes that they have large affinity with.

The segmentation quality assessment is given in Table 4.3. The difference of the quantitative results between the biased normalized cut compared with our approach is not as high as the biomedical experiments because of the additional colour image information and the lack of the shape variation information as we use only a single prior, but still our technique can improve the others results.

	Colour images			
	New	PG	BNC_i	BNC_{ic}
Distance (voxel)	4.63	8.59	5.07	4.75
Overlap	0.57	0.57	0.53	0.54
Sensitivity	0.67	0.90	0.65	0.65
Specificity	0.77	0.43	0.76	0.76
Similarity	0.71	0.71	0.68	0.69

Table 4.3: Average performance measures for colour images, for the proposed approach (New), (PG) Partial Grouping, (BNC_i) Intensity based-Biased Ncut, (BNC_{ic}) Intervening contour based-Bias Ncut.

4.5 Conclusions

We presented a new algorithm to add shape prior knowledge into the normalized cut formulation to improve the performance and make it a robust candidate for clinical purposes. The prior is integrated into the cost function without the inclusion of hard constraints. Multiple priors are easily incorporated into the framework. Hence, shape models can be directly included into the framework to model the typical variations

of the prior. Experiments suggest that our method is robust and accurate for different medical imaging modalities even when the image is noisy or has low contrast. Moreover, we show that the proposed method outperforms the state-of-the art of normalized cuts with prior knowledge.

Chapter 5

Non-Euclidean Basis-based Level Sets with Shape Prior

5.1 Introduction

The radial basis functions (RBFs) were originally used as a primary tool for interpolation of multivariate scattered data because it does not require any underlying mesh for interpolation. The ability of these methods to allow arbitrary scattered data, ease of generalization to several space dimensions, and spectral accuracy has made RBFs particularly popular in different types of applications including surface reconstruction, terrain modeling, fluid-structure interaction, the numerical solution of partial differential equations, kernel learning, and parameter estimation. Furthermore, these applications come from such different fields as applied mathematics, computer science, biology, geology, engineering, and even business studies [101].

In 1990, RBFs were extended by Kansa to approximate parabolic, hyperbolic and elliptic Partial Differential Equation (PDE) systems in the field of computational fluid dynamics [102]. Recently, RBFs have received much attention for solving PDE systems [103, 104] as well as for image segmentation in combination with level sets. With this approach, instead of partial differential equations, surface evolution is governed by a set of ordinary differential equations, which is much easier to solve, reinitialization is no longer necessary, and more complex topological changes are read-

ily achievable [105]. In conventional level set methods, active contours or surfaces are not able to create topological changes away from the zero level set where the deformable contours or surfaces are embedded [104, 106, 107]. Thus, the level sets, for example, could miss holes inside objects. In order to solve accurately the associated PDEs using finite difference methods, the implicit function is required to be smooth and remain so during the evolution of the interface [106]. Therefore, reinitialization is usually needed in order to achieve numerical stability. Alternative methods without reinitialization have been proposed, but they often require dedicated extension of the speed function defined on the contour [106]. Summing up, the main potential interests of using the RBF in the framework of level-sets are [108]:

1. the RBF scheme allows an overall control of the level set (i.e., over the whole computational domain of the level set) with a reasonable computational cost in contrast to the conventional finite difference narrow band implementations.

2. Since the RBF representation of the level set is parametric, it is relatively easy to constrain the propagation via constraints on the parameters. Such constraints may be used to avoid the usual reinitialization step of the level set. As a consequence, the solution is topologically more flexible, since it may develop new contours which are difficult to obtain when the narrow-band/reinitialization strategy is used.

3. The smoothness of the solution is implicitly enforced, through the intrinsic smoothness of the underlying RBF representation. The RBF formulation, thus, does not need to include the usual curvature term in the propagation equation.

4. The obtained solution is continuous, the degree of continuity being imposed by the type of RBF chosen for the application.

Several methods combining level sets with RBFs have recently been published in the image segmentation field. For example, Wimmer et al. used RBFs to reconstruct a surface to initialize a level set algorithm [109]. Turk et al. [110] introduced constraint points to model the implicit level set surface using RBFs, which were applied to

implicit active contour modeling by Morse et al. [111]. Gelas et al. [112] applied compactly supported RBFs to image segmentation and introduced prior knowledge of shape by placing the RBF centers quasi-uniformly over an uncertainty area. Bernard et al. [113] formulated the segmentation problem in a Maximum Likelihood framework using the Generalized Gaussian as a priori distribution and minimizing the resulting functional using a multiphase level set and RBF model. Slabaugh et al. [114] proposed to use anisotropic Gaussian kernels and optimized their orientation as well as their weight, position and scales. Mory et al. [115] proposed to build RBFs according to image features using non-Euclidean distance and incorporated prior information by casting inside/outside labels as linear inequality constraints.

In spite of the potential advantages, the combination of RBFs and level sets is relatively new in image segmentation. Implementation of the approach can be complex and it is still unclear what benefit and drawback this combination can potentially bring for an application. In this Chapter, we detail a new framework for biomedical image segmentation by combining the level set method with shape prior and non-Euclidean RBFs to arrive at an accurate and efficient image segmentation method. Existing approaches to integrating shape prior into RBFs include RBFs center placement approaches which have been tested on synthetic data [112]. We propose a new approach to integrating shape prior to RBFs using a statistical shape prior and introduce the non-Euclidean RBF within the optimization framework of Gelas et al. [112]. Additionally, we report experimental results applied on real data as well as critical analysis of the combination.

5.2 Radial Basis Functions

A RBF is a circularly-symmetric function centered in a particular point. The sum of RBFs is typically used to approximate functions. A function f can be approximated by a linear combination of translated and scaled RBFs centered around N points x_i traditionally called collocation points:

$$f(x) = \sum_{i=1}^{N} \lambda_i \varphi\left(||x - x_i||\right) \tag{5.1}$$

where φ is the radially-symmetric non-negative kernel, x_i is the position of the known values h_i in the interpolation and λ_i is the weight of the RBF positioned at that point. The norm $||\ ||$ is usually the Euclidean distance although other distance functions are also possible. The coefficients λ are computed by solving:

$$H \cdot [\lambda] = [h] \tag{5.2}$$

where h is the column vector whose elements are $\{h_i\}$ and H is a square matrix of size N:

$$H = \begin{pmatrix} \varphi\left(||x_1 - x_1||\right) & \varphi\left(||x_1 - x_2||\right) & \varphi\left(||x_1 - x_3||\right) & \dots & \varphi\left(||x_1 - x_N||\right) \\ \varphi\left(||x_2 - x_1||\right) & \varphi\left(||x_2 - x_2||\right) & \varphi\left(||x_2 - x_3||\right) & \dots & \varphi\left(||x_2 - x_N||\right) \\ \varphi\left(||x_3 - x_1||\right) & \varphi\left(||x_3 - x_2||\right) & \varphi\left(||x_3 - x_3||\right) & \dots & \varphi\left(||x_3 - x_N||\right) \\ \vdots & \vdots & \vdots & \vdots & \vdots \\ \varphi\left(||x_N - x_1||\right) & \varphi\left(||x_N - x_2||\right) & \varphi\left(||x_N - x_3||\right) & \dots & \varphi\left(||x_N - x_N||\right) \end{pmatrix}$$

Thereby, the coefficients are obtained by solving the system of N linear equations given by:

$$\begin{pmatrix} \varphi\left(||x_1 - x_1||\right) & \varphi\left(||x_1 - x_2||\right) & \varphi\left(||x_1 - x_3||\right) & \dots & \varphi\left(||x_1 - x_N||\right) \\ \varphi\left(||x_2 - x_1||\right) & \varphi\left(||x_2 - x_2||\right) & \varphi\left(||x_2 - x_3||\right) & \dots & \varphi\left(||x_2 - x_N||\right) \\ \varphi\left(||x_3 - x_1||\right) & \varphi\left(||x_3 - x_2||\right) & \varphi\left(||x_3 - x_3||\right) & \dots & \varphi\left(||x_3 - x_N||\right) \\ \vdots & \vdots & \vdots & \vdots & \vdots \\ \varphi\left(||x_N - x_1||\right) & \varphi\left(||x_N - x_2||\right) & \varphi\left(||x_N - x_3||\right) & \dots & \varphi\left(||x_N - x_N||\right) \end{pmatrix} \begin{pmatrix} \lambda_1 \\ \lambda_2 \\ \lambda_3 \\ \vdots \\ \lambda_N \end{pmatrix} = \begin{pmatrix} h_1 \\ h_2 \\ h_3 \\ \vdots \\ h_N \end{pmatrix}$$

Given the coefficients, the unknown points are approximated by Equation 5.1. The typical radially-symmetric non-negative kernels φ include: Gaussian $\varphi(r) = e^{r^2\sigma^2}$, and Compactly Support Wendland $\varphi(r) = (1 - r^4) + (4r + 1)$ where $r = ||x - x_i||$.

By using other kernels, it may be necessary to add a first-degree polynomial P into Equation 5.1 to ensure positive definiteness of the radial basis functions.

5.3 Level Set with Radial Basis Functions

The problem of segmentation of one object is typically handled by the evolution of a level set whose steady state partitions the image into two regions delimiting the object boundaries [108]. The level set propagation can be achieved by considering the front evolving along the normal direction according to a localized speed function. It can be expressed as follows:

$$\frac{\partial f(x,t)}{\partial t} = V(x,t) \cdot \delta_\epsilon(f(x,t)) \tag{5.3}$$

where V is a velocity function and δ_ϵ is a regularized version of the Dirac function given as $\delta_\epsilon(x) = \frac{1}{\pi\epsilon\cdot(1+(\frac{x}{\epsilon})^2)}$ where ϵ is a real positive constant. Some authors modified the evolution equation Equation 5.3 by substituting δ by ∇. This operation does not affect the steady state solution and remove stiffness near the zero level set [112]. For more details refer to Chapter 2.4.

The evaluation of f for any point x can be expressed as the product of one line vector $\varphi(x)$ and a column vector λ:

$$f(x) = \varphi(x) \cdot \lambda \tag{5.4}$$

Then, RBF formulation follows straightforwardly from the application of the RBF decomposition to the implicit function f in Equation 5.4, by assuming that space and time are separable [112]. In such case, this naturally leads to the following decomposition:

$$f(x,t) = \varphi(x) \cdot \lambda(t) \tag{5.5}$$

Replacing the Function 5.5 into Equation 5.3, we get the following expression:

$$H \cdot \frac{\partial \lambda(t)}{\partial t} = B(\lambda(t), t) \tag{5.6}$$

where $H_{ij} = \varphi(||x_i - x_j||)$, $B = V(x_i, t) \cdot \delta(\varphi(x_i) \cdot \lambda(t))$ and λ are the scalar weights.

To solve the ordinary differential equation, Gelas et al. [112] apply a first order forward Euler method to Equation 5.6 which lead them to:

$$\lambda^{n+1} = \lambda^n - \tau \cdot H^{-1} \cdot B^n(\lambda^n) \tag{5.7}$$

In case of using positive definite functions such as gaussian RBFs or Compact Wendland RBFs , the associated matrix H is also positive definite. Thereby, H can be decomposed by Cholesky decomposition $H = L \cdot L^T$ where L is a lower triangular matrix and the evolution equation of the level set becomes:

$$\begin{cases} L \cdot u^n = B^n(\tilde{\lambda}^n) \\ L^T \cdot v^n = u^n \\ \lambda^{n+1} = \lambda^n - \tau \cdot v^n \end{cases}$$

where u, v are the unknowns obtained by solving the corresponding equations, n indicates the iteration and τ is the time step. In order to avoid RBF coefficients keeping growing when the implicit interface reaches a stable solution, the implicit function is bounded by applying a normalization on RBF coefficients which bounds $||\lambda^n||_1$. The evolution equation becomes:

$$\begin{cases} H = L \cdot L^\top \\ L \cdot u^n = B^n(\tilde{\lambda}^{n-1}) \\ L^\top \cdot v^n = u^n \\ \lambda^n = \tilde{\lambda}^{n-1} - \tau \cdot v^n \\ \tilde{\lambda}^n = \frac{\alpha}{||\lambda^n||_1} \cdot \lambda^n \end{cases} \tag{5.8}$$

where H is decomposed by Cholesky decomposition, n indicates the iteration, α is a positive constant and τ is the time step. For the proposed method, we use $\tau = 5$ and $\alpha = 10$. The parameters were chosen empirically.

5.4 Non-Euclidean Radial Basis

The Euclidean distance is commonly used in RBFs. As a consequence RBF kernels are of spherical shape, resulting over-smoothed shape representation. In order to improve the segmentation, Mory et al. [115] proposed to use an image-dependent non-Euclidean distance to build the RBF kernel. In so doing, the RBFs are no longer spherical but determined by the image features. The new formulation is as follows:

$$\varphi_i(x) = \varphi\left(\frac{||x - x_i||_{g_i}}{\sigma_i}\right) \tag{5.9}$$

where σ_i are the scales and g_i is the metric function chosen.

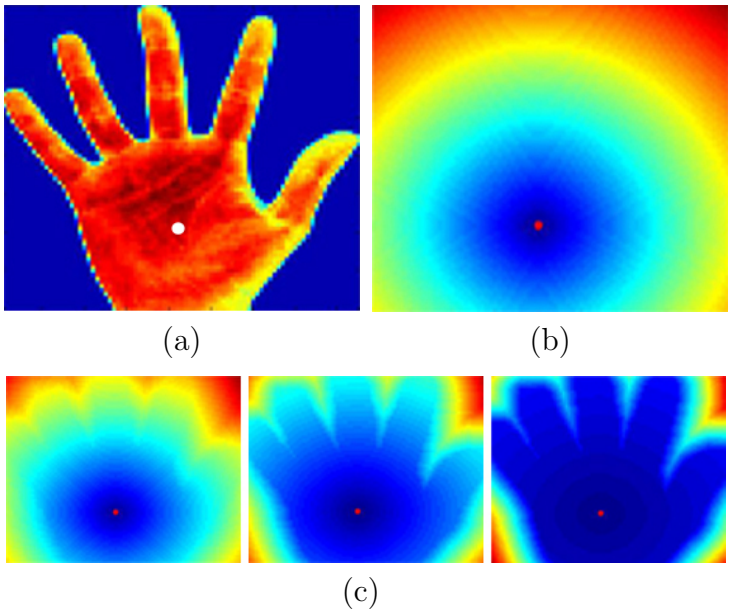

Figure 5-1: The effect of the non-Euclidean distance metric. (a) Original Image with a RBF center in the middle. (b) Spherical-shaped RBF with $\beta = 0$. (c) Increasing the non-Euclidean part of the metric from left to right with $\beta > 0$.

The authors define the non-Euclidean distance from a physical interpretation of fronts propagating from the center points x_i with the image-dependent speed function $1/g_i$. In case of $g_i = 1$, the Euclidean case is re-obtained. In the simple case of piecewise constant images, $g_i(x) = 1 + \beta(I(x) - I(x_i))^2$ can be chosen. The metric g_i recommended for general cases is the local image intensity distribution P_{x_i}, estimated in the neighborhood of x_i: $g_i(x) = 1 - \beta log P_{x_i}(I(x))$ where $\beta > 0$ controls the non-

Euclidean part of the metric. The effect of the metric is illustrated in Fig. 5-1 where we show that bigger β is the better the basis function will adapt to the image features. A fast marching method is used to calculate the geodesic distances between collocation points x_i with speed function $1/g_i$ (Section 5.5).

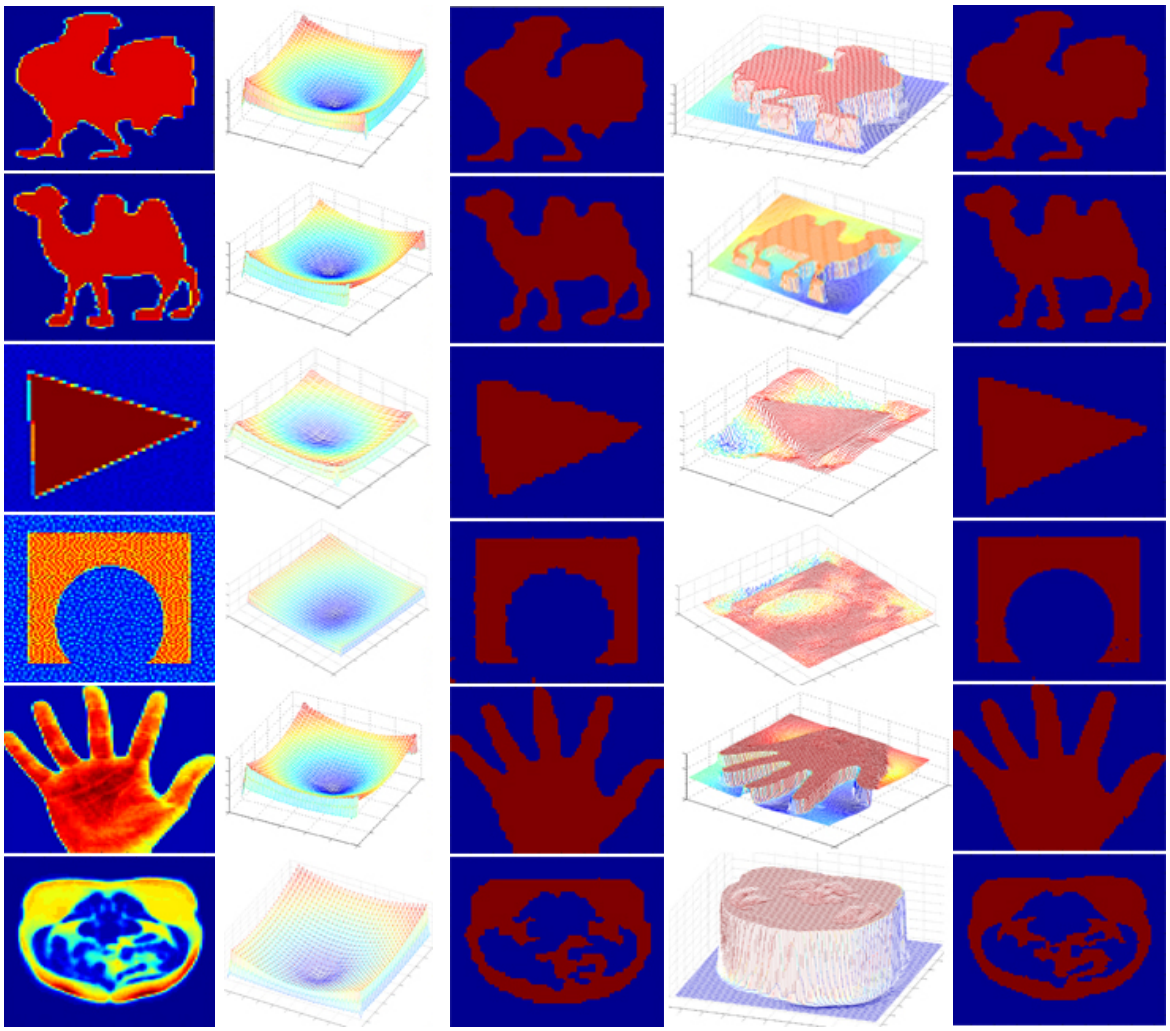

Figure 5-2: Comparison of Non-Euclidean RBFs versus Euclidean RBFs. (a) Original image. (b) Initial level set using Euclidean Distance. (c) Segmentation using Euclidean RBFs. (d) Initial level set using Non-Euclidean Distance. (e) Segmentation using Non-Euclidean RBFs.

A comparison between Euclidean RBFs and Non-Euclidean basis functions is shown in Fig. 5-2. We observe that the initial level set using non-radial basis captures the image features of the image giving a more accurate segmentation than the Eu-

clidean RBFs. The metric used for the comparison is $g_i(x) = abs(1+\beta(I(x)-I(x_i)))$.

By construction, such non-Euclidean distances are meaningful only in a local neighborhood of the control point x_i. As a consequence, the function φ must not only be nonnegative as in the Euclidean case but also monotonically decreasing, to discard meaningless high distance values [115] . The localization of each basis function φ_i in Equation 5.9 can then be controlled by its scale parameter σ_i. A Gaussian kernel would be a valid choice, but Mory et al. use for complexity reasons the C2 compactly-supported Wendland function [101].

$$\forall a \in R,\ \ \varphi(a) = \begin{cases} (a-1)^4(4a+1)\ \ if\ \ a \leq 1 \\ 0\ \ otherwise \end{cases} \tag{5.10}$$

5.5 Fast Marching

Fast Marching Method (FMM) introduced by Sethian [116], is an efficient algorithm to compute geodesic distances by solving an eikonal equation in discrete domain, where 4-neighbors of a voxel are used to estimate actual distances. The general expression of the eikonal equation in 2D is as follows:

$$|\nabla T(x,y)| = F(x,y) \tag{5.11}$$

where $T(x,y)$ is the arrival time of the curve at grid point (x,y) and F is the speed function. If F is constant over the whole domain, the solution of the eikonal equation is exactly the Euclidean distance [117].

For an upwind scheme, the approximation to the gradient $|\nabla T(x,y)|$ is written as:

$$max(D_{ij}^{-x}T, -D_{ij}^{+x}T, 0)^2 + max(D_{ij}^{-y}T, -D_{ij}^{+y}T, 0)^2 = \frac{1}{F_{ij}^2} \tag{5.12}$$

where $F_{ij} \equiv F(i\triangle x, j\triangle y)$, $D_{ij}^{-x}T \equiv \frac{T_{ij}-Ti-1j}{h}$ and $D_{ij}^{+x}T \equiv \frac{T_{i+1j}-T_{1j}}{h}$ are the standard backward and forward derivative approximation with h representing the grid spacing; equivalently for D_{ij}^{+y} and D_{ij}^{-y} [118].

The solution of Equation 5.12 can be efficiently computed with the fast marching method. Each grid point can be classified as *known* where the arrival time at x will not be changed, *narrow band* when the arrival time may be changed later and far where the arrival time at x is not yet computed. Given these definitions, the simple fast method is computed by:

- Mark an initial set of grid points as known. Mark as narrow band, all points neighbouring known points. Mark all other grid points as far.
- LOOP: Among all narrow band points, extract the point with minimum arrival time and tag it to known.
- Find its nearest neighbours that are either far or narrow band and label them as narrow band if they are not known.
- Update their arrival times of all neighbours by solving Equation 5.12.
- Go back to LOOP.

Although the FMM gives a stable and consistent solution to the eikonal equation, it still has two limitations [119]. First, the computational complexity of the method is high because it stores the solutions in a narrow band that is implemented using a sorted heap data structure. The complexity of maintaining the heap is $O(log\ n)$, where n is the total number of grid points. Therefore, the total complexity of the method is $O(n\ log\ n)$. Second, the method uses only the information of the four adjacent neighbors at each grid point, thus ignoring the information provided by diagonal points. As a consequence, the FMM suffers from a large numerical error along diagonal directions [119]. Several methods have been developed to improve the FMM in terms of computational efficiency [120, 121] or accuracy [122, 123]. In our implementation, we use multi-stencils fast marching (MSFM) which covers the 8-neighbors of a point [119] but any other implementation is suitable for the problem.

5.6 Region and Shape Prior Definition

Having defined the methods for explicitly representing the level set surface using RBFs, we need to incorporate it into the level set evolution to guide the segmentation towards the object of interest. The Chan-Vese active contour model [124] is a popular method for region-based level set segmentation which aims at partitioning an image into regions with piecewise constant intensity. As shown in Section 2.4, the energy functional of the Chan Vese model is:

$$E(C) = \lambda_0 \int_{insideC} |I - \mu_{in}|^2 d\Omega + \lambda_1 \int_{outsideC} |I - \mu_{out}|^2 d\Omega + \gamma_1 length(C) + \nu_2 Area(C) \tag{5.13}$$

where I is the original image, μ_{in} and μ_{out} are the average values of pixels inside and outside the curve C respectively, and the last two terms are regularizers terms that put constraints on the length and the area of the curve.

In a level set framework, C is the zero level set of a Lipschitz function $\phi(x)$. Therefore, the unknown variable C can be replaced by the unknown variable $\phi(x)$, and the energy function in Equation 5.13 becomes:

$$E(\phi) = \lambda_0 \int_{insideC} |I-\mu_{in}|^2 H(\phi) d\Omega + \lambda_1 \int_{outsideC} |I-\mu_{out}|^2 (1-H(\phi)) d\Omega + \gamma_1 length(\phi) + \nu_2 Area(\phi) \tag{5.14}$$

where H is the heaviside function. Keeping μ_{in} and μ_{out} fixed at the same time, the Chan-Vese energy functional can be minimized with respect to $\phi(x)$, and deduced the associated Euler-Lagrange equation for $\phi(x)$. Parameterizing the descent direction by an artificial time t, we can obtain the corresponding variational level set formulation as follows:

$$\frac{\partial \phi}{\partial t} = \delta_\epsilon [\gamma_1 \cdot \kappa - \nu_2 - (I - \mu_{in})^2 + (I - \mu_{out})^2] \tag{5.15}$$

where I is the original image and κ is the curvature term which makes the curve

smooth weighted by γ. Due to the intrinsic smoothness of the RBF formulation, the smoothing term is omitted, and the velocity term referred in the Equation 5.6 is simplified as follows:

$$V(x,t) = -(I(x) - c_1)^2 + (I(x) - c_2)^2 \tag{5.16}$$

The Chan Vese method is suitable for piecewise-constant images but for more general cases, it can be replaced by a maximum-likelihood criterion: $V(x,t) = r_1 - r_2$ where $r_i(I(x)) = -logP_i(I(x))$ and P_1 and P_2 are the intensity distributions [115].

In addition to the region term, we require prior information to guide the evolution of the level set surface to a certain shape. To do so, we compute the average shape of a training set and then align it using registration to the target image [125] as shown in Fig. 5-3. As a result, we obtain a spatial prior giving a probabilistic map for the foreground P_{in} and background P_{out}. The energy functional for the spatial prior is given by:

$$E_{shape} = -\int_\Omega H(\phi) logP_{in}(x)dx - \int_\Omega (1 - H(\phi)) logP_{out}(x)dx \tag{5.17}$$

The shape energy functional can be minimized with respect to $\phi(x)$ and results in the following velocity:

$$V_{shape}(x) = -\left(log\frac{P_{in}(x)}{P_{out}(x)}\right) \tag{5.18}$$

Combining region and shape information, the velocity term becomes:

$$V(x) = \mu_1(-(I(x) - c_1)^2 + (I(x) - c_2)^2) - \mu_2\left(log\frac{P_{in}(x)}{P_{out}(x)}\right) \tag{5.19}$$

where the first term is the Chan-Vese model that can be replaced by any other suitable model according to the image features [115, 126] and the second term is the shape prior term where P_{in} and P_{out} are the probability of the foreground and background respectively, obtained from the probabilistic map. μ_1 and μ_2 are the weights for the region and prior terms respectively and are chosen empirically.

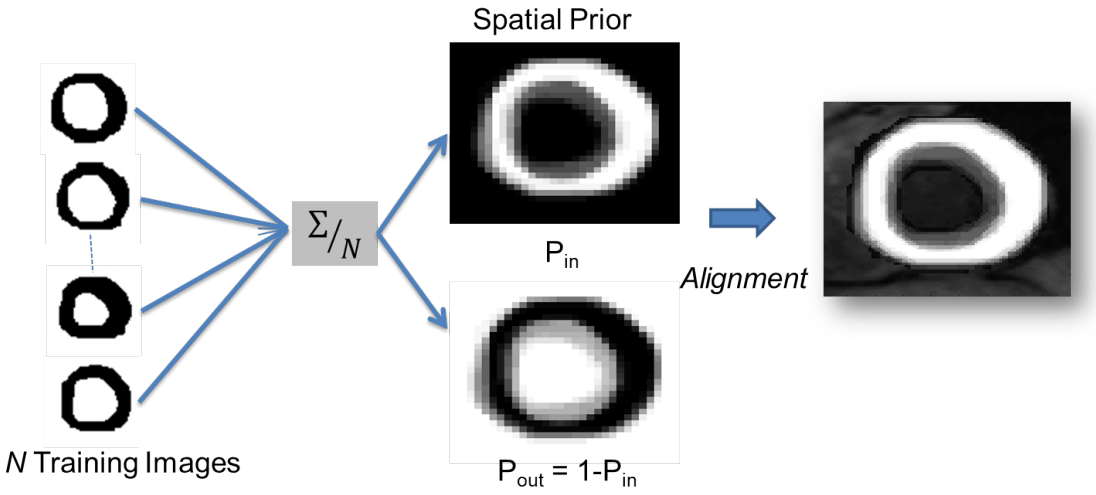

Figure 5-3: Example of spatial shape prior. Given N training images an average image is computed as a spatial prior which is aligned to the target image and used as a probabilistic map for the level set segmentation.

5.7 Validation

We test our method for segmentation of the myocardium using fifteen datasets of different patients. Each dataset contains among 26 to 57 frames. The ground truth is manually segmented by an expert. Experimental results with our method are compared with the common level set technique and that obtained using Euclidean RBFs. All methods use the same energy terms and a single circle as an initial contour. In order to make the level set more flexible topologically, we did not implement the narrow band, the computation of a band around the front instead of the whole image, to cope not only with the endocardium but also the epicardium. This causes an increase of the computational complexity of the algorithm, whereas the radial basis representation allows more flexible topologies without adding additional cost. The parameter setting for the Non-Euclid and Euclid RBFs are: $\tau = 5$ and $\alpha = 10$ from the evolution Equation 5.8 of the weights, $\sigma_i = 6.98$ from Equation 5.9 with a compactly-supported Wendland kernel and the center points are equally distributed, e.g., one point every three points. For the level set function, $\tau = 1.5$. All parameters have been empirically chosen for all techniques. According to the experiments, the level

set method produced more outliers due to image noise. The level set re-initialization also caused problems in some cases misplacing the final segmentation. On the other hand, the level set gave sharper segmentations than the Euclidean RBFs in some images. However, this trend is reversed when more RBFs are added, or when non-Euclidean RBFs are used. Non-Euclidean RBFs follow the image features better, allowing closer initialization and therefore better convergence. Some examples using the non-Euclidean basis function with shape prior are shown in Fig. 5-4. Moreover, some of the artifacts described above are shown in Fig. 5-5.

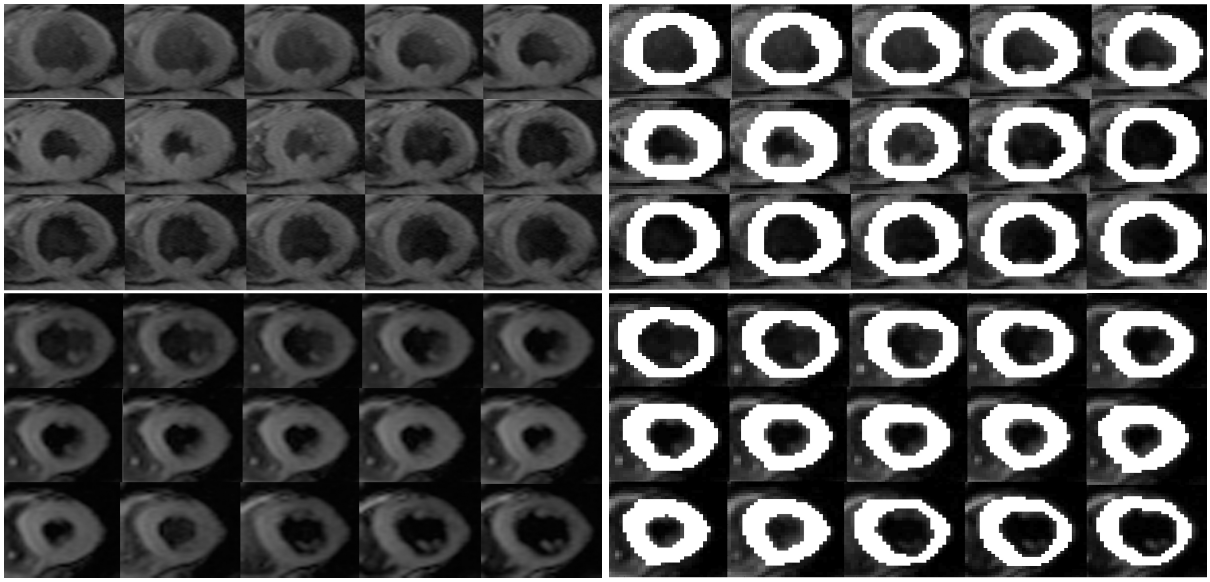

(a) (b)

Figure 5-4: Segmentation of the myocardium using our approach with two different patients: a) Original data sets. b) Segmentation in white.

To quantify the segmentation quality assessment, we compute different performance measures: point to mesh distance which indicates the distance between the segmentation and the ground truth and overlap, sensitivity, specificity and similarity [1].

Table 5.1 summarizes the average performance for all methods showing a better performance with our approach. The distance between the ground truth and the

[1]The performance measures are defined as [127]: $Overlap = \frac{TP}{TP+FN+FP}$, $Sensitivity = \frac{TP}{TP+FN}$, $Specificity = \frac{TN}{TN+FP}$ and $Similarity = \frac{2TP}{2TP+FN+FP}$ where TP and FP stand for true positive and false positive and TN and FN for true negative and false negative.

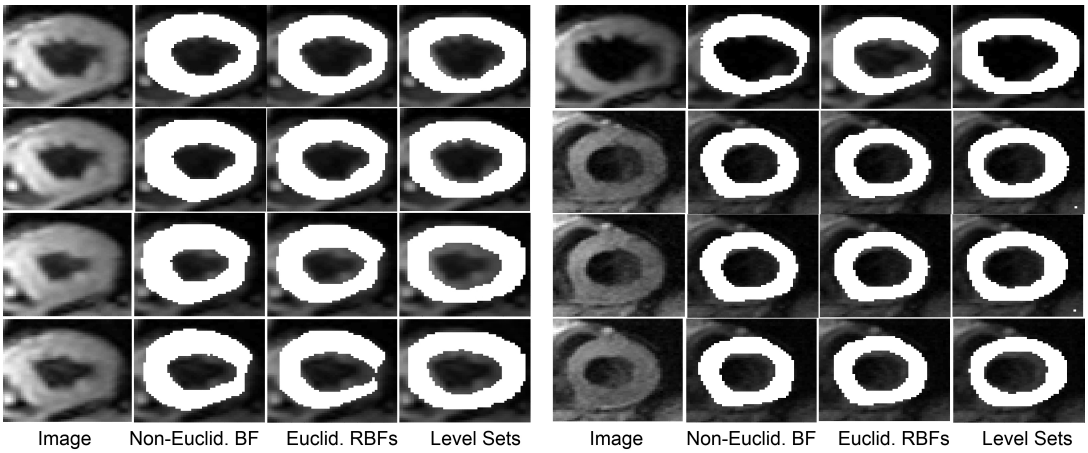

Figure 5-5: Comparison of methods: Non-Euclidean Basis Functions, Euclidean RBFs and the ordinary Level Sets.

segmentation is smaller and the metric values for similarity, overlap and sensitivity (fraction of pixels belonging to the myocardium correctly detected) are higher. And for specificity (fraction of pixels not belonging to the myocardium correctly detected), according to our experiments, the results remain the same for all methods.

	Myocardium		
	New	Euclid. RBFs	Level Sets
Distance (voxel)	0.76	0.77	0.79
Overlap	0.76	0.74	0.72
Sensitivity	0.80	0.77	0.75
Specificity	0.98	0.98	0.98
Similarity	0.87	0.85	0.84

Table 5.1: Average performance measures for cardiac sequences, for the proposed approach (New), the Euclidean radial basis approach, and the level set method.

5.8 Conclusion

We have implemented a new framework for medical image segmentation using a statistical shape-based level set method represented as a combination of non-Euclidean RBFs. The use of RBFs avoids using reinizialitation which reshapes the level set

as the interface signed distance function to avoid developing of steep regions in the implicit function. The reinitialization scheme increases the computational cost and reduces the topological flexibility of the method since it prevents the level set from creating new zero level components far away from the initial interface. Using radial basis, reinizialization is no longer required and allows more topological flexibility. By using non-Euclidean distance, basis functions can incorporate image features giving more accurate results. Non-Euclidean RBFs follow the image features better, allowing closer initialization and therefore better convergence. To guide the segmentation to the object of interest, we use a probabilistic map obtained as an average shape of training data and incorporate it into the level set function as a prior information. Combining the probabilistic map with a region data term, we obtain the final segmentation. The experiments suggest that our method is robust and accurate even for noisy and low contrast images.

Chapter 6

Conclusions

The goal of this work is to develop novel segmentation techniques for myocardial segmentation in cardiac MRI. But they can be used for any other type of biomedical images or natural images as shown in the experimental validation of the corresponding approaches.

The first approach presented is based on normalized cuts using prior. The proposed method seeks the normalized cut while maximizing the association of the prior within a group and the disassociation between the other. Our main contribution is that the prior is included in the cost function without the inclusion of hard constraints. Furthermore, depending on the application, the method does not require the inclusion of spatial relationships, because they are already in the prior term and it can be extended easily to deal with multiple priors applying principal component analysis. The method has been validated on biomedical and natural images giving satisfactory results as well as compared with the state-of-the-art of normalized cut approaches with prior giving a more robust and accurate segmentation.

The second method proposed uses a statistical shape-based level set method represented as a combination of non-Euclidean RBFs. The explicit RBF representation of the level set allows the level set evolution to be represented as ordinary differential equations and reinitialization is no longer required. Furthermore, by using non-Euclidean distance, basis functions can incorporate image features giving more accurate results. To guide the segmentation to the object of interest, we use a proba-

bilistic map obtained as an average shape of training data. Experimental results and a comparison with the traditional level sets and the RBFs-based level sets are reported obtaining a more sharpen and accurate segmentation with the proposed approach.

Our future work includes an extension to 3D of the techniques presented in this work.

Authors' Contribution

International Journals

Esmeralda Ruiz Pujadas and Marco Reisert. Shape-based Normalized Cuts using spectral relaxation for biomedical segmentation. *Transactions on Image Processing*. (ACCEPTED; Impact Factor: 3.19).

International Conferences

Esmeralda Ruiz Pujadas, Martin Buechert, Michael Weiner and Stathis Hadjidemetriou. Normalized Cuts method for biomedical MRI segmentation. In *proceedings of International Society for Magnetic Resonance in Medicine*, 2011.

Esmeralda Ruiz Pujadas and Marco Reisert. Review and analytical discussion of cardiac segmentation. In *proceedings of International Society for Magnetic Resonance in Medicine*, 2012.

Esmeralda Ruiz Pujadas and Marco Reisert. Image segmentation using normalized cuts with multiple priors. In *proceedings of SPIE Medical Imaging*, pp. 866937-1 - 866937-7, 2013.

Esmeralda Ruiz Pujadas and Marco Reisert. Image segmentation using normalized cuts with multiple priors. In *proceedings of Medical Imaging using Bio-inspired and Soft Computing*, pp. 147 - 151, 2013. ISBN: 978-84-695-7710-3.

Esmeralda Ruiz Pujadas, Marco Reisert and Li Bai. Non-Euclidean basis function based level set segmentation with statistical shape prior. In *proceedings of IEEE Engineering in Medicine and Biology Society*, pp. 5123 - 5126, 2013.

Esmeralda Ruiz Pujadas, Marco Reisert and Li Bai. Semi-automated segmentation for 2D cardiac MR images using level set and analytical issues of the method. In *proceedings of German Chapter: International Society for Magnetic Resonance in Medicine*, 2013. ISSN: 1863-6365.

International Journals (Submitted)

Esmeralda Ruiz Pujadas, Marco Reisert and Li Bai. Level Set segmentation based on non-euclidean basis functions and spatial shape prior. *Computer Vision and Image Understanding.*

Esmeralda Ruiz Pujadas. Review of medical image segmentation methods. *Computer Vision and Image Understanding.*

Bibliography

[1] J. Malmivuo and R. Plonsey, *Bioelectromagnetism: principles and applications of bioelectric and biomagnetic fields*. Oxford University Press, 1995.

[2] G. J. Tortora and B. H. Derrickson, *Principles of anatomy and physiology*. Wiley, 2006.

[3] C. Petitjean and J.-N. Dacher, "A review of segmentation methods in short axis cardiac MR images," *Medical Image Analysis*, vol. 15, no. 2, pp. 169–184, 2011.

[4] T. Albrecht, M. Lüthi, and T. Vetter, "Deformable models," in *Encyclopedia of Biometrics*, Springer, 2009.

[5] D. Cremers, T. Pock, K. Kolev, and A. Chambolle, "Convex relaxation techniques for segmentation, stereo and multiview reconstruction," MIT Press, 2011.

[6] L. Hao, "Registration-based segmentation of medical images," *School of Computing National University of Singapore*, 2006.

[7] V. Grau, A. Mewes, M. Alcaniz, R. Kikinis, and S. K. Warfield, "Improved watershed transform for medical image segmentation using prior information," *Medical Imaging, IEEE Transactions on*, vol. 23, no. 4, pp. 447–458, 2004.

[8] M. Kass, A. Witkin, and D. Terzopoulos, "Snakes: Active contour models," *International journal of computer vision*, vol. 1, no. 4, pp. 321–331, 1988.

[9] J. Pardo, D. Cabello, and J. Heras, "A snake for model-based segmentation of biomedical images," *Pattern Recognition Letters*, vol. 18, no. 14, pp. 1529–1538, 1997.

[10] J. L. Troutman, *Variational calculus with elementary convexity*. Springer-Verlag, 1983.

[11] A. A. Amini, T. E. Weymouth, and R. C. Jain, "Using dynamic programming for solving variational problems in vision," *Pattern Analysis and Machine Intelligence, IEEE Transactions on*, vol. 12, no. 9, pp. 855–867, 1990.

[12] L. D. Cohen and I. Cohen, "Finite-element methods for active contour models and balloons for 2-d and 3-d images," *Pattern Analysis and Machine Intelligence, IEEE Transactions on*, vol. 15, no. 11, pp. 1131–1147, 1993.

[13] S. T. Acton and N. Ray, "Biomedical image analysis: segmentation," *Synthesis Lectures on Image, Video, and Multimedia Processing*, vol. 4, no. 1, pp. 1–108, 2009.

[14] C. F. Gerald and P. O. Wheatley, *Numerical analysis*. Addison-Wesley, 2003.

[15] C. Xu and J. L. Prince, "Gradient vector flow: A new external force for snakes," in *Computer Vision and Pattern Recognition, 1997. Proceedings., 1997 IEEE Computer Society Conference on*, pp. 66–71, IEEE, 1997.

[16] E. Angelini, Y. Jin, and A. Laine, "State of the art of level set methods in segmentation and registration of medical imaging modalities," in *Handbook of Biomedical Image Analysis*, pp. 47–101, Springer, 2005.

[17] F. Leitner and P. Cinquin, "Dynamic segmentation: Detecting complex topology 3d-object," in *Engineering in Medicine and Biology Society, 1991. Vol. 13: 1991., Proceedings of the Annual International Conference of the IEEE*, pp. 295–296, IEEE, 1991.

[18] T. McInerney and D. Terzopoulos, "Topologically adaptable snakes," in *Computer Vision, 1995. Proceedings., Fifth International Conference on*, pp. 840–845, IEEE, 1995.

[19] R. Szeliski, D. Tonnesen, and D. Terzopoulos, "Modeling surfaces of arbitrary topology with dynamic particles," in *Computer Vision and Pattern Recognition, 1993. Proceedings CVPR'93., 1993 IEEE Computer Society Conference on*, pp. 82–87, IEEE, 1993.

[20] V. Caselles, F. Catté, T. Coll, and F. Dibos, "A geometric model for active contours in image processing," *Numerische Mathematik*, vol. 66, no. 1, pp. 1–31, 1993.

[21] S. Osher and J. A. Sethian, "Fronts propagating with curvature-dependent speed: algorithms based on hamilton-jacobi formulations," *Journal of computational physics*, vol. 79, no. 1, pp. 12–49, 1988.

[22] D. Adalsteinsson, *A fast level set method for propagating interfaces*. PhD thesis, Citeseer, 1994.

[23] R. Malladi, J. A. Sethian, and B. C. Vemuri, "Shape modeling with front propagation: A level set approach," *Pattern Analysis and Machine Intelligence, IEEE Transactions on*, vol. 17, no. 2, pp. 158–175, 1995.

[24] S. Kichenassamy, A. Kumar, P. Olver, A. Tannenbaum, and A. Yezzi, "Gradient flows and geometric active contour models," in *Computer Vision, 1995. Proceedings., Fifth International Conference on*, pp. 810–815, IEEE, 1995.

[25] V. Caselles, R. Kimmel, and G. Sapiro, "Geodesic active contours," *International journal of computer vision*, vol. 22, no. 1, pp. 61–79, 1997.

[26] J. S. Suri, K. Liu, S. Singh, S. N. Laxminarayan, X. Zeng, and L. Reden, "Shape recovery algorithms using level sets in 2-d/3-d medical imagery: a state-of-the-art review," *Information Technology in Biomedicine, IEEE Transactions on*, vol. 6, no. 1, pp. 8–28, 2002.

[27] D. Mumford and J. Shah, "Boundary detection by minimizing functionals," *Image understanding*, pp. 19–43, 1988.

[28] T. Chan and L. Vese, "An active contour model without edges," in *Scale-Space Theories in Computer Vision*, pp. 141–151, Springer, 1999.

[29] A. Tsai, A. Yezzi Jr, and A. S. Willsky, "Curve evolution implementation of the mumford-shah functional for image segmentation, denoising, interpolation, and magnification," *Image Processing, IEEE Transactions on*, vol. 10, no. 8, pp. 1169–1186, 2001.

[30] T. F. Cootes, C. J. Taylor, D. H. Cooper, J. Graham, *et al.*, "Active shape models-their training and application," *Computer vision and image understanding*, vol. 61, no. 1, pp. 38–59, 1995.

[31] S. C. Mitchell, B. P. F. Lelieveldt, R. J. van der Geest, H. G. Bosch, J. Reiver, and M. Sonka, "Multistage hybrid active appearance model matching: segmentation of left and right ventricles in cardiac MR images," *Medical Imaging, IEEE Transactions on*, vol. 20, no. 5, pp. 415–423, 2001.

[32] Y. Boykov and O. Veksler, "Graph cuts in vision and graphics: Theories and applications," in *Handbook of mathematical models in computer vision*, pp. 79–96, Springer, 2006.

[33] Y. Boykov and V. Kolmogorov, "An experimental comparison of min-cut/max-flow algorithms for energy minimization in vision," *Pattern Analysis and Machine Intelligence, IEEE Transactions on*, vol. 26, no. 9, pp. 1124–1137, 2004.

[34] Y. Boykov, O. Veksler, and R. Zabih, "Fast approximate energy minimization via graph cuts," in *Computer Vision, 1999. The Proceedings of the Seventh IEEE International Conference on*, vol. 1, pp. 377–384, IEEE, 1999.

[35] T. Rohlfing, R. Brandt, R. Menzel, D. B. Russakoff, and C. R. Maurer Jr, "Quo vadis, atlas-based segmentation?," in *Handbook of Biomedical Image Analysis*, pp. 435–486, Springer, 2005.

[36] J. P. W. Pluim, J. B. A. Maintz, and M. A. Viergever, "Mutual-information-based registration of medical images: a survey," *Medical Imaging, IEEE Transactions on*, vol. 22, no. 8, pp. 986–1004, 2003.

[37] C. Studholme, D. L. Hill, D. J. Hawkes, *et al.*, "An overlap invariant entropy measure of 3d medical image alignment," *Pattern recognition*, vol. 32, no. 1, pp. 71–86, 1999.

[38] P. Viola and W. M. Wells III, "Alignment by maximization of mutual information," in *Computer Vision, 1995. Proceedings., Fifth International Conference on*, pp. 16–23, IEEE, 1995.

[39] F. Maes, A. Collignon, D. Vandermeulen, G. Marchal, and P. Suetens, "Multimodality image registration by maximization of mutual information," *Medical Imaging, IEEE Transactions on*, vol. 16, no. 2, pp. 187–198, 1997.

[40] M. Lorenzo-Valdés, G. I. Sanchez-Ortiz, R. Mohiaddin, and D. Rueckert, "Atlas-based segmentation and tracking of 3d cardiac MR images using non-rigid registration," in *Medical Image Computing and Computer-Assisted Intervention–MICCAI 2002*, pp. 642–650, Springer, 2002.

[41] J. Lötjönen, S. Kivistö, J. Koikkalainen, D. Smutek, K. Lauerma, *et al.*, "Statistical shape model of atria, ventricles and epicardium from short-and long-axis MR images.," *Medical image analysis*, vol. 8, no. 3, p. 371, 2004.

[42] X. Zhuang, D. Hawkes, W. Crum, R. Boubertakh, S. Uribe, D. Atkinson, P. Batchelor, T. Schaeffter, R. Razavi, and D. Hill, "Robust registration between cardiac MRI images and atlas for segmentation propagation," in *Medical Imaging*, pp. 691408–691408, International Society for Optics and Photonics, 2008.

[43] A. Blake, P. Kohli, and C. Rother, *Markov random fields for vision and image processing*. The MIT Press, 2011.

[44] S. Boyd and L. Vandenberghe, *Convex Optimization*. Cambridge University Press, 2004.

[45] T. Pock, A. Chambolle, D. Cremers, and H. Bischof, "A convex relaxation approach for computing minimal partitions," in *Computer Vision and Pattern Recognition, 2009. CVPR 2009. IEEE Conference on*, pp. 810–817, IEEE, 2009.

[46] J. L. Carter, *Dual methods for total variation-based image restoration*. PhD thesis, University of California Los Angeles, 2001.

[47] T. F. Chan, G. H. Golub, and P. Mulet, "A nonlinear primal-dual method for total variation-based image restoration," *SIAM Journal on Scientific Computing*, vol. 20, no. 6, pp. 1964–1977, 1999.

[48] A. Chambolle, "An algorithm for total variation minimization and applications," *Journal of Mathematical imaging and vision*, vol. 20, no. 1-2, pp. 89–97, 2004.

[49] A. Chambolle, D. Cremers, and T. Pock, *A convex approach for computing minimal partitions*. Citeseer, 2008.

[50] T. F. Chan, S. Esedoglu, and M. Nikolova, "Algorithms for finding global minimizers of image segmentation and denoising models," *SIAM Journal on Applied Mathematics*, vol. 66, no. 5, pp. 1632–1648, 2006.

[51] Y. Lu, P. Radau, K. Connelly, A. Dick, and G. A. Wright, "Segmentation of left ventricle in cardiac cine MRI: An automatic image-driven method," in *Functional Imaging and Modeling of the Heart*, pp. 339–347, Springer, 2009.

[52] M. Fradkin, C. Ciofolo, B. Mory, G. Hautvast, and M. Breeuwer, "Comprehensive segmentation of cine cardiac MR images," in *Medical Image Computing and Computer-Assisted Intervention–MICCAI 2008*, pp. 178–185, Springer, 2008.

[53] S. OBrien, O. Ghita, and P. Whelan, "Segmenting the left ventricle in 3d using a coupled asm and a learned non-rigid spatial model," *The MIDAS Journal*, vol. 49, 2009.

[54] M. Jolly, "Fully automatic left ventricle segmentation in cardiac cine MR images using registration and minimum surfaces," in *MICCAI 2009 Workshop on Cardiac MR Left Ventricle Segmentation Challenge. MIDAS Journal*, 2009.

[55] C. Constantinides, Y. Chenoune, N. Kachenoura, E. Roullot, E. Mousseaux, A. Herment, and F. Frouin, "Semi-automated cardiac segmentation on cine magnetic resonance images using gvf-snake deformable models," *The MIDAS Journal-Cardiac MR Left Ventricle Segmentation Challenge*, 2009.

[56] D. G. Kendall, "The diffusion of shape," *Advances in applied probability*, vol. 9, no. 3, pp. 428–430, 1977.

[57] I. Dryden and K. Mardia, *Statistical analysis of shape*. Wiley, 1998.

[58] M. B. Stegmann and D. D. Gomez, "A brief introduction to statistical shape analysis," *Informatics and Mathematical Modelling, Technical University of Denmark, DTU*, 2002.

[59] P. H. Schönemann, "A generalized solution of the orthogonal procrustes problem," *Psychometrika*, vol. 31, no. 1, pp. 1–10, 1966.

[60] P. H. Schönemann and R. M. Carroll, "Fitting one matrix to another under choice of a central dilation and a rigid motion," *Psychometrika*, vol. 35, no. 2, pp. 245–255, 1970.

[61] C. Goodall, "Procrustes methods in the statistical analysis of shape," *Journal of the Royal Statistical Society. Series B (Methodological)*, pp. 285–339, 1991.

[62] F. L. Bookstein, "Landmark methods for forms without landmarks: localizing group differences in outline shape," in *Mathematical Methods in Biomedical Image Analysis, 1996., Proceedings of the Workshop on*, pp. 279–289, IEEE, 1996.

[63] K. Pearson, "Liii. on lines and planes of closest fit to systems of points in space," *The London, Edinburgh, and Dublin Philosophical Magazine and Journal of Science*, vol. 2, no. 11, pp. 559–572, 1901.

[64] H. Hotelling, "Analysis of a complex of statistical variables into principal components," *Journal of educational psychology*, vol. 24, no. 6, p. 417, 1933.

[65] I. Jolliffe, *Principal component analysis*. Wiley Online Library, 2005.

[66] S. M. Holland, *Principal components analysis (PCA)*. University of Georgia, 2008.

[67] T.-W. Lee, *Independent component analysis*. Springer, 1998.

[68] L. Deng, N.-n. Rao, and G. Wang, "Active shape model of combining PCA and ICA: Application to facial feature extraction," *Journal of Electronic Science and Technology of China*, vol. 4, no. 2, pp. 115–117, 2006.

[69] M. Üzümcü, A. F. Frangi, J. H. Reiber, and B. P. Lelieveldt, "Independent component analysis in statistical shape models," in *Society of Photo-Optical Instrumentation Engineers (SPIE) Conference Series*, vol. 5032, pp. 375–383, 2003.

[70] M. Üzümcü, A. F. Frangi, M. Sonka, J. H. Reiber, and B. P. Lelieveldt, "ICA vs. PCA active appearance models: Application to cardiac MR segmentation," in *Medical Image Computing and Computer-Assisted Intervention-MICCAI 2003*, pp. 451–458, Springer, 2003.

[71] A. Hyvärinen and E. Oja, "A fast fixed-point algorithm for independent component analysis," *Neural computation*, vol. 9, no. 7, pp. 1483–1492, 1997.

[72] A. J. Bell and T. J. Sejnowski, "An information-maximization approach to blind separation and blind deconvolution," *Neural computation*, vol. 7, no. 6, pp. 1129–1159, 1995.

[73] J.-F. Cardoso, "High-order contrasts for independent component analysis," *Neural computation*, vol. 11, no. 1, pp. 157–192, 1999.

[74] A. F. Frangi, J. H. Reiber, B. P. Lelieveldt, *et al.*, "Independent component analysis in statistical shape models," in *Medical Imaging 2003*, pp. 375–383, International Society for Optics and Photonics, 2003.

[75] M. Üzümcü, *Constrained Segmentation of Cardiac MR Image Sequences*. PhD thesis, Universiteit Leiden, 1976.

[76] M. Bressan and J. Vitrià, "Independent modes of variation in point distribution models," in *Visual Form 2001*, pp. 123–134, Springer, 2001.

[77] T. F. Cootes and C. J. Taylor, "A mixture model for representing shape variation," *Image and Vision Computing*, vol. 17, no. 8, pp. 567–573, 1999.

[78] T. Heap and D. Hogg, "Improving specificity in pdms using a hierarchical approach.," in *BMVC*, 1997.

[79] R. Bowden, T. Mitchell, and M. Sarhadi, "Reconstructing 3d pose and motion from a single camera view," in *BMVC*, vol. 98, pp. 904–913, 1998.

[80] S. Romdhani, S. Gong, A. Psarrou, *et al.*, "A multi-view nonlinear active shape model using kernel PCA," in *BMVC*, vol. 10, pp. 483–492, 1999.

[81] E.-J. Ong and S. Gong, "A dynamic human model using hybrid 2D-3D representations in hierarchical PCA space," in *In BMVC*, Citeseer, 1999.

[82] M. Yamazaki and F. Sidney, "Local image descriptors using supervised kernel ICA," *IEICE transactions on information and systems*, vol. 92, no. 9, pp. 1745–1751, 2009.

[83] Q. Liu, J. Cheng, H. Lu, and S. Ma, "Modeling face appearance with nonlinear independent component analysis," in *Automatic Face and Gesture Recognition, 2004. Proceedings. Sixth IEEE International Conference on*, pp. 761–766, IEEE, 2004.

[84] J. Shi and J. Malik, "Normalized cuts and image segmentation," *Pattern Analysis and Machine Intelligence, IEEE Transactions on*, vol. 22, no. 8, pp. 888–905, 2000.

[85] J. Carballido-Gamio, S. Belongie, and S. Majumdar, "Normalized cuts in 3-d for spinal MRI segmentation," *Medical Imaging, IEEE Transactions on*, vol. 23, no. 1, pp. 36–44, 2004.

[86] A. Brun, H. Knutsson, H. Park, M. Shenton, and C. Westin, "Clustering fiber traces using normalized cuts," *Medical Image Computing and Computer-Assisted Intervention–MICCAI 2004*, pp. 368–375, 2004.

[87] S. Yu and J. Shi, "Grouping with bias," *Advances in Neural Information Processing Systems*, vol. 14, pp. 1327–1334, 2001.

[88] S. Yu and J. Shi, "Segmentation given partial grouping constraints," *Pattern Analysis and Machine Intelligence, IEEE Transactions on*, vol. 26, no. 2, pp. 173–183, 2004.

[89] A. Eriksson, C. Olsson, and F. Kahl, "Normalized cuts revisited: A reformulation for segmentation with linear grouping constraints," in *Computer Vision, 2007. ICCV 2007. IEEE 11th International Conference on*, pp. 1–8, IEEE, 2007.

[90] S. Maji, N. Vishnoi, and J. Malik, "Biased normalized cuts," in *Computer Vision and Pattern Recognition (CVPR), 2011 IEEE Conference on*, pp. 2057–2064, IEEE, 2011.

[91] D. Tolliver, G. Miller, and R. Collins, "Corrected laplacians: Closer cuts and segmentation with shape priors," in *Computer Vision and Pattern Recognition, 2005. CVPR 2005. IEEE Computer Society Conference on*, vol. 2, pp. 92–98, IEEE, 2005.

[92] W. Cai, J. Wu, and A. Chung, "Shape-based image segmentation using normalized cuts," in *Image Processing, 2006 IEEE International Conference on*, pp. 1101–1104, IEEE, 2006.

[93] M. Everingham, L. Van Gool, C. K. I. Williams, J. Winn, and A. Zisserman, "The pascal visual object classes (voc) challenge," *International Journal of Computer Vision*, vol. 88, pp. 303–338, June 2010.

[94] S. Maji, N. Vishnoi, and J. Malik, "Biased normalized cuts code." `http://www.cs.berkeley.edu/~smaji/projects/biasedNcuts/`. Accessed: Oct. 21, 2011.

[95] P. V. Hough, "Machine analysis of bubble chamber pictures," in *International Conference on High Energy Accelerators and Instrumentation*, vol. 73, 1959.

[96] B. A. Jung, B. W. Kreher, M. Markl, and J. Hennig, "Visualization of tissue velocity data from cardiac wall motion measurements with myocardial fiber tracking: principles and implications for cardiac fiber structures," *European journal of cardio-thoracic surgery*, vol. 29, no. Supplement 1, pp. S158–S164, 2006.

[97] D. Grosgeorge, C. Petitjean, J. Caudron, J. Fares, and J. Dacher, "Automatic cardiac ventricle segmentation in MR images: a validation study," *International journal of computer assisted radiology and surgery*, vol. 6, no. 5, pp. 573–581, 2011.

[98] "Segmentation validation engine." `http://sve.bmap.ucla.edu/instructions/metrics/dice/`. Accessed: Jan. 11, 2012.

[99] L. Bourdev and J. Malik, "Poselets: Body part detectors trained using 3d human pose annotations," in *Computer Vision, 2009 IEEE 12th International Conference on*, pp. 1365–1372, IEEE, 2009.

[100] L. Bourdev and J. Malik, "Poselets and their applications in high-level computer vision." `http://www.cs.berkeley.edu/~lbourdev/poselets/`. Accessed: Jul. 12, 2012.

[101] H. Wendland, *Scattered data approximation*, vol. 17. Cambridge University Press, 2005.

[102] E. Kansa, "Multiquadrics. a scattered data approximation scheme with applications to computational fluid-dynamics ii," *Computers and mathematics with applications*, vol. 19, no. 8, pp. 147–161, 1990.

[103] T. Cecil, J. Qian, and S. Osher, "Numerical methods for high dimensional hamilton–jacobi equations using radial basis functions," *Journal of Computational Physics*, vol. 196, no. 1, pp. 327–347, 2004.

[104] S. Wang, K. Lim, B. Khoo, and M. Wang, "An extended level set method for shape and topology optimization," *Journal of Computational Physics*, vol. 221, no. 1, pp. 395–421, 2007.

[105] X. Xie and M. Mirmehdi, "Radial basis function based level set interpolation and evolution for deformable modelling," *Image and Vision Computing*, vol. 29, no. 2, pp. 167–177, 2011.

[106] X. Xie and M. Mirmehdi, "Implicit active model using radial basis function interpolated level sets.," in *BMVC*, pp. 1–10, 2007.

[107] R. Ramlau and W. Ring, "A mumford–shah level-set approach for the inversion and segmentation of x-ray tomography data," *Journal of Computational Physics*, vol. 221, no. 2, pp. 539–557, 2007.

[108] A. Gelas, O. Bernard, D. Friboulet, and R. Prost, "Compactly supported radial basis functions based collocation method for level-set evolution in image segmentation," *IEEE Transactions on Image Processing*, vol. 16, no. 7, pp. 1873–1887, 2007.

[109] A. Wimmer, G. Soza, and J. Hornegger, "Two-stage semi-automatic organ segmentation framework using radial basis functions and level sets," *3D Segmentation in The Clinic: A Grand Challenge*, pp. 179–188, 2007.

[110] G. Turk and J. O'brien, "Modelling with implicit surfaces that interpolate," *ACM Transactions on Graphics (TOG)*, vol. 21, no. 4, pp. 855–873, 2002.

[111] B. Morse, W. Liu, T. Yoo, and K. Subramanian, "Active contours using a constraint-based implicit representation," in *ACM SIGGRAPH 2005 Courses*, p. 252, ACM, 2005.

[112] A. Gelas, J. Schaerer, O. Bernard, D. Friboulet, P. Clarysse, I. Magnin, and R. Prost, "Radial basis functions collocation methods for model based level-set segmentation," in *IEEE International Conference on Image Processing, 2007. ICIP 2007.*, vol. 2, pp. II–237, IEEE, 2007.

[113] O. Bernard, B. Touil, A. Gelas, R. Prost, and D. Friboulet, "A rbf-based multiphase level set method for segmentation in echocardiography using the statistics of the radiofrequency signal," in *IEEE International Conference on Image Processing, 2007. ICIP 2007.*, vol. 3, pp. 157–160, IEEE, 2007.

[114] G. Slabaugh, Q. Dinh, and G. Unal, "A variational approach to the evolution of radial basis functions for image segmentation," in *IEEE Conference on Computer Vision and Pattern Recognition, 2007. CVPR'07.*, pp. 1–8, IEEE, 2007.

[115] B. Mory, R. Ardon, A. Yezzi, and J. Thiran, "Non-euclidean image-adaptive radial basis functions for 3d interactive segmentation," in *IEEE 12th International Conference on Computer Vision, 2009*, pp. 787–794, IEEE, 2009.

[116] J. A. Sethian, "A fast marching level set method for monotonically advancing fronts," *Proceedings of the National Academy of Sciences*, vol. 93, no. 4, pp. 1591–1595, 1996.

[117] L. Bertelli, B. Sumengen, and B. Manjunath, "Redundancy in all pairs fast marching method," in *Image Processing, 2006 IEEE International Conference on*, pp. 3033–3036, IEEE, 2006.

[118] C. Moenning and N. A. Dodgson, "Fast marching farthest point sampling," in *Proc. Eurographics*, 2003.

[119] M. S. Hassouna and A. A. Farag, "Multistencils fast marching methods: A highly accurate solution to the eikonal equation on cartesian domains," *Pattern Analysis and Machine Intelligence, IEEE Transactions on*, vol. 29, no. 9, pp. 1563–1574, 2007.

[120] S. Kim, "An O(N) level set method for eikonal equations," *SIAM journal on scientific computing*, vol. 22, no. 6, pp. 2178–2193, 2001.

[121] G. Sapiro, L. Yatziv, and A. Bartesaghi, *O (N) Implementation of the Fast Marching Algorithm*. Minnesota University, 2005.

[122] J. A. Sethian, *Level set methods and fast marching methods: evolving interfaces in computational geometry, fluid mechanics, computer vision, and materials science*, vol. 3. Cambridge University Press, 1999.

[123] P.-E. Danielsson and Q. Lin, "A modified fast marching method," in *Image Analysis*, pp. 1154–1161, Springer, 2003.

[124] T. Chan and L. Vese, "Active contours without edges," *IEEE Transactions on Image Processing*, vol. 10, no. 2, pp. 266–277, 2001.

[125] X. Lin, B. Cowan, and A. Young, "Model-based graph cut method for segmentation of the left ventricle," in *27th Annual International Conference of the Engineering in Medicine and Biology Society, 2005. IEEE-EMBS 2005.*, pp. 3059–3062, IEEE, 2006.

[126] N. Paragios and R. Deriche, "Geodesic active regions for supervised texture segmentation," in *Computer Vision, 1999. The Proceedings of the Seventh IEEE International Conference on*, vol. 2, pp. 926–932, IEEE, 1999.

[127] L. Chaabane and M. Abdelouahab, "Evaluation of the segmentation by multispectral fusion approach with adaptive operators: Application to medical images," *Evaluation*, vol. 2, no. 9, 2011.